Revision 2

Exploring the potential of Raman spectroscopy for crystallochemical analyses of complex hydrous silicates: I. Amphiboles

Lisa Leißner,[1] Jochen Schlüter,[2] Ingo Horn,[3] and Boriana Mihailova[1,*]

[1]Fachbereich Geowissenschaften, Universität Hamburg, Grindelallee 48, D-20146 Hamburg, Germany

[2]Centrum für Naturkunde, Mineralogisches Museum, Universität Hamburg, Grindelallee 48, D-20146 Hamburg, Germany

[3]Institut für Mineralogie, Leibniz Universität Hannover, Callinstr. 3, D-30167 Hannover, Germany

[*]corresponding author: boriana.mihailova@uni-hamburg.de

Running title: Crystal chemistry of amphiboles by Raman spectroscopy

ABSTRACT

Detailed Raman spectroscopic and electron microprobe studies of 33 amphibole ($AB_2C_5T_8O_{22}W_2$, C_5=$M1_2M2_2M3$) crystals from 6 amphibole subgroups were performed to check whether the Raman scattering arising from OH bond stretching vibrations can be used for the identification and site-occupancy analysis of amphiboles. The following results can be gained from this study: (i) C-site Mg and Fe^{2+} on the M1M1M3 triplet linked to the W-site OH^- lead to two-mode behavior of the OH bond stretching mode: up to four Raman peaks separated by ~16 cm^{-1} from each other can be observed and their fractional intensities can be used to quantify the concentration of M1M1M3 chemical species as well as to estimate the overall C-site occupancy by Mg and Fe^{2+}; (ii) the

coexistence of Mg and Fe^{2+} on the B site also leads to two-mode behavior but the peak splitting is only ~3 cm^{-1}; the fractional intensities of these split components can be used to refine the B-site occupation factors of Mg and Fe^{2+}. (iii) the presence of B-site Li, Na, and Ca results in one-mode behavior of the OH Raman peaks, i.e., slight shift of the peak positions depending on the concentration of distinct chemical species. The total replacement of B-site Ca by Na should reduce the peak positions by 6.5 cm^{-1}, whereas that of Li by ~13 cm^{-1}; (iv) A-site occupancy leads to strong broadening as well as to a strong shift of the OH peaks toward higher wavenumbers. The full width at half maximum (FWHM) of OH-stretching peaks associated with filled A sites is ~ 22 cm^{-1} versus ~8 cm^{-1} for OH peaks associated with vacant A sites. For ^{T}Al-poor amphiboles the M1M1M3-OH peaks shift towards higher wavenumbers by ~37 cm^{-1} in the case of ^{W}OH - A-cation - ^{W}F species and by 60 cm^{-1} in the case of ^{W}OH - A-cation - ^{W}OH species with respect to the peak position for ^{W}OH - A-vacancy - ^{W}OH species; (v) high content of ^{C}Al, i.e., ^{M2}Al > 1 atom per formula unit (apfu) seems to lead to one-mode behavior and an additional shift towards lower wavenumbers by ~4 cm^{-1}; (vi) OH peaks with FWHM ~ 30-40 cm^{-1} may indicate high-content of ^{T}Al (1 or 2 apfu), which can be verified by analyzing the FWHM of the Raman peak near 670 cm^{-1}, generated by vibrations of bridging oxygen atoms in TO_4 rings; (vii) the W-site occupancy factor of the OH groups can be estimated using the intensity ratio η between the total Raman scattering generated by OH bond stretching and the Raman peak near 670 cm^{-1} generated by TO_4-ring vibrations; a small value of η (< 0.09) combined with the presence of strong Raman scattering near 750-780 cm^{-1} is indicative of oxo-amphiboles. Guidelines for non-specialists how to use the Raman scattering of OH bond stretching modes for "rough" but preparation-free, non-destructive and easy-to-handle crystallochemical quantitative analyses of amphiboles are suggested.

Keywords: amphibole, Raman spectroscopy, electron microprobe analysis.

INTRODUCTION

Amphiboles are hydrous silicates with a complex chemical composition, having several crystallographic sites that can be occupied by various chemical elements. The general formula of amphiboles is $AB_2C_5T_8O_{22}W_2$, with A = □ (vacancy), Na^+, K^+, Ca^{2+}, Pb^{2+}, Li^+, B = Na^+, Ca^{2+}, Mn^{2+}, Fe^{2+}, Mg^{2+}, Li^+; C = Mg^{2+}, Fe^{2+}, Mn^{2+}, Al^{3+}, Fe^{3+}, Mn^{3+}, Cr^{3+}; Ti^{4+}, Li^+; T = Si^{4+}, Al^{3+}, Ti^{4+}, Be^{2+}; W = OH^-, O^{2-}, F^-, Cl^- (Hawthorne et al. 2012). The structure of amphiboles is composed of chains of 6-membered rings of TO_4 tetrahedra attached via the apical oxygen atoms to strips of edge-sharing CO_6 octahedra (Fig. 1a). The C site is comprised of three crystallographically distinguishable sites, M1, M2 and M3, and the W site is shared between two $M1O_6$ and one $M3O_6$ octahedra (Fig. 1). The B sites, which are also commonly labeled as M4 and may comprise two subsites M4 and M4' (Bottazzi et al., 1999), link the strips of TO_4-rings and CO_6 octahedra in-plane. A more precise site nomenclature should be M(1), M(2), M(3), and M(4), as in the IMA report by Hawthorne et al. (2012). However, for the sake of conciseness we use the labelling M1, M2, M3, and M4 throughout the whole paper. The A sites are between two W sites, interconnecting the strips in the perpendicular direction (Fig.1b)

Amphiboles occur in most rock types, from mafic to felsic rocks, and are stable over a significant pressure and temperature range. Therefore they can be used as geothermo- and geobarometers (Holland and Blundy 1994). Amphiboles appear also as gemstones or asbestos (Vinx 2008; Deer et al. 1980). Hence, identification and crystalochemical analysis of amphiboles is important in geosciences as well as in environmental sciences. Thus it is desirable to have a quick and easy-to-handle analytical method with μm-scale spatial resolution to identify amphibole subgroups or even amphibole species. Raman spectroscopy has the great potential to be used for this purpose because (i) the set of Raman-active modes obey strict symmetry-related selection rules, i.e., the structure type can immediately be fingerprinted, (ii) the phonon

wavenumbers (the peak positions) depend on the masses and interatomic force constants of the atoms involved in the corresponding mode, i.e., Raman spectra carry essential chemical information, which allows for discriminating different species within the same mineral group, (iii) integrated intensities of the Raman peaks depend on the number of the corresponding "dynamical units" and hence, the relative intensity can be indicative of the concentration of specific chemical species; (iv) Raman spectroscopy does not require sample powdering or any special sample preparation and can be applied to micrometer-sized amphibole grains in crude rock samples as well as in polished sections and even in glass-covered thin sections, which is rather beneficial as compared to infrared spectroscopy.

The chemical composition on the non-tetrahedral sites in amphiboles can be studied by analyzing directly the vibrations related to A-, B-, and C-site cations as well as indirectly, by analyzing the influence of non-tetrahedral cations on the vibrations of the common chemical species in amphiboles: the silicate rings and the hydroxyl groups. The different chemical surroundings of the silicate rings/hydroxyl groups may lead to two-mode and/or one-mode behavior. In the former case more Raman peaks than predicted by group-theory analysis are observed and their fractional intensities correlate with the chemical variation, whereas in the latter case the chemical variation results in a quantitatively related shift of the peak position (Chang and Mitra 1971). The O-H bond stretching is a high-energy vibration (~3500-3700 cm^{-1}) and therefore even subtle relative changes in the mode wavenumber should result in absolute changes in the peak positions that are large enough to be detected. The latter is quite promising for establishing a correlation between the Raman peak parameters and the crystal chemistry of amphiboles.

Raman spectroscopy has been applied to amphiboles but most of the studies are focused on the framework phonon modes below 1200 cm^{-1}. There are only few Raman spectroscopic studies considering the OH-stretching modes (Chen et al. 2004; Kloprogge et al. 2001; Su et al. 2009; Wang et al. 1988). Wang et al. (1988) performed Raman

analysis of the OH-range in cummingtonite. Chen et al. (2004) studied the crystal chemistry of Chinese jade by Raman spectroscopy of OH-stretching modes in combination with proton induced x-ray emission analysis. Kloprogge et al. (2001) studied the Raman spectra of Li-containing holmquistite. All three studies showed that a determination of Fe-Mg content of the amphiboles due to the OH-stretching modes is possible, similar to that already established by powder infrared spectroscopy. Su et al. (2009) studied zoned amphiboles by infrared and Raman spectroscopy and reported a good agreement between both methods. However a detailed and systematic Raman-scattering study of the OH-stretching range with a number of samples of different amphibole subgroups and complex chemistry, like that performed by Apopei and Buzgar (2010) for the range 200-1200 cm^{-1}, is still missing. In addition, the OH-stretching range of amphibole samples with a filled A site has not been studied so far. Therefore the objective of this study was to analyze the Raman scattering arising from OH groups in a large variety of natural amphiboles covering the main amphibole subgroups to explore the potential of Raman spectroscopy for non-destructive crystal-chemical analysis of amphiboles. Due to the enormous diversity of amphiboles, this study has been focused on Mn-poor amphiboles without Al on the tetrahedral position. Thus the initial selection of the crystals aimed to assemble a suit of ^{W}OH-dominant amphibole samples from various subgroups that have negligible amount of Mn and ^{T}Al.

MATERIALS AND METHODS

Samples

33 amphibole samples from 6 out of 9 subgroups (see Fig. 2) have been studied: magnesium-iron-manganese (samples S1-S6), calcium (samples S7-S18), sodium-calcium (S19-S21), sodium (samples S22-S29), and lithium amphiboles (samples S30, S31) as well as oxo-amphiboles (samples S32, S33). Most of the samples are from the

collection of the Mineralogical Museum, Centrum für Naturkunde (CeNak), the University of Hamburg. Sample S26 was kindly provided by the Museum für Naturkunde Berlin and samples S16 and S27 were kindly provided by the Mineralogical Museum of the TU Bergakademie Freiberg. Details about the sample localities are given by Leißner (2014).

Analytical methods

All samples were analyzed by Raman spectroscopy and electron microprobe. Raman scattering experiments were conducted with a Horiba Jobin-Yvon T64000 triple-monochromator spectrometer equipped with an Olympus BX41 confocal microscope and Symphony liquid-N_2-cooled charge-coupled device (CCD) detector. Spectra were recorded in backscattering geometry, i.e. reflection mode. The Raman spectra for the majority of the samples were excited with the green line of an Ar^+ laser (λ = 514.532 nm) and collected in the spectral ranges 15-1215 cm^{-1} and 2600-3800 cm^{-1}. Due to the high continuum photoluminescence background when a visible laser was used, the Raman spectra of samples S1, S8, and S9 were also collected with a CdHe laser emitting at 325 nm. Visible Raman spectroscopy was performed using holographic gratings of 1800 grooves/mm and a 50× objective, whereas ultraviolet (UV) Raman spectroscopy was conducted with holographic gratings of 2400 grooves/mm and a 40× objective. The spectral resolution achieved with a green laser and UV laser was ~2 cm^{-1} and ~3 cm^{-1}, respectively. The accuracy in determining the peak positions was 0.35 cm^{-1} for the 514.5-nm laser line and 1 cm^{-1} for the 325-nm laser line. Amphiboles exhibit typical prismatic morphology and the direction of the crystal elongation is along the prism axis, which is parallel to the strips of TO_4-rings and CO_6 octahedra (see Fig. 1). In general, the crystal orientation influences the intensities of the Raman peaks. Hence, parallel polarized and cross polarized Raman spectra were measured in backscattering geometry from two different orientations of the sample: with the polarization of the incident light parallel and

perpendicular to the direction of crystal elongation. These scattering geometries were chosen because the amphibole crystal habit allows to orient the crystal very easily that way, including small-sized mineral grains embedded in a crude rock and asbestos samples. Preliminary measurements showed that the rotation of the crystal about the prismatic axis may have significant influence on the relative Raman intensities mainly in the range 900-1000 cm^{-1}, which originates from Si-O bond stretching, but has negligible effect on the relative intensities of the O-H bond stretching modes. All Raman spectra were collected from raw natural surfaces. The use of a microscope and visible/UV laser made possible to focus on a flat area of linear size ~2-3 μm. The Raman spectra in the range 2600-3800 cm^{-1} were baseline corrected with polynomial functions for the continuum photoluminescence background and fitted with pseudo-Voigt functions $PV = q * Lorentz + (1-q) * Gauss$ with $q \in [0,1]$, to determine the peak positions, full widths at half maximum (FWHMs), and integrated intensities.

Electron microprobe analyses (EMPA) were performed with a Cameca SX-100 SEM system using a wavelength-dispersive detector. The energy of the electron beam was 15 keV and the beam current was 20 nA. The diameter of the beam spot on the sample surface was kept to 10 μm. The following standards were used: LiF for F, albite for Na, MgO for Mg, Al_2O_3 for Al, andradite for Si, Ca and Fe, vanadinite for Cl, orthoclase for K, $MnTiO_3$ for Ti and Mn, Cr_3O_3 for Cr, Zn-containing glass for Zn, $SrTiO_3$ for Sr, and Ba-containing glass for Ba. The acquisition times were 60 s for F, Na, Cl, K, Ti, Cr, Mn, Zn, Sr and Ba, 30 s for Ca, 20 s for Mg, Al and Fe, and 10 s for Si. Measurements were performed in 25-50 points for each sample, which ensured statistical standard deviations allowing for composition uncertainty in the calculated chemical formulas ~0.01 or better.

Two samples (S28, S29) that showed ambiguous results in the chemical formulas calculated on the basis of EMPA data were additionally characterized by laser-ablation inductively-coupled-plasma mass spectrometry (LA ICP-MS). The experiments were

conducted with a ThermoFisher Element XR magnet sector field mass spectrometer in low resolution connected to a SpectraPhysics Solstice based femtosecond laser ablation system operating in the deep UV at 194 nm. Details on the experimental set up are given by Horn et al. (2006) and Albrecht et al. (2014). The content of Li, B, Na, Mg, Al, Si, K, Ca, Ti, Mn, and Fe was probed by LA ICP-MS, using a He flushed cell with a volume of 35 cm^3. For each sample data were collected from three spatial regions sized approximately 20×20 μm. Each spatial region was subjected to a raster analysis with an ablation spot size of 35 μm.

A few samples (S17, S32, S33) exhibited overall Raman scattering below 1200 cm^{-1} differing from that of the majority of the samples; these samples were examined by powder X-ray diffraction (XRD) (Philips X'Pert diffractometer, Cu K_α radiation) to verify their amphibole structure. One sample, S1, the polarized Raman spectra of which suggested plausible orthorhombic symmetry of the structure, was subjected to single-crystal X-ray diffraction analysis using a Nonius Kappa diffractometer with a CCD detector and Mo K_α radiation.

RESULTS AND DISCUSSION

Chemical composition from EMPA and ICP-MS

The EMPA results were first checked for too high or too low wt% of oxide totals. The typical oxide totals for amphiboles should be around 97-98 wt% because of the non-measureable amount of hydrogen (Martin 2007). However fluoro-amphiboles may have oxide totals of 100 wt%, whereas presence of Fe^{3+} may lower the oxide totals to about 96 wt% if the total amount of Fe is calculated as FeO. High Li^+ content may further lower the totals to ~94 wt%. Thus data points with oxide totals lower than 94 wt% were excluded in the subsequent statistic averaging because they may represent surface defects. Then the calculations of the chemical formulas, including Fe^{3+} recalculations, have been done following the procedures described by Leake et al. (2003) and in the

appendix of Hawthorne et al. (2012). The obtained total weight sums for some samples suggested the presence of Li^{+}, the content of which was calculated by adjusting the total weight sums to 100 wt% presuming a fully occupied W (Hawthorne et al. 2012).

The samples were named according to the new amphibole nomenclature (Hawthorne et al. 2012), using the program AMPH2012 developed by Oberti et al. (2012). The chemical formulas of the samples are given in Table 1. Sample S1 was named anthophyllite rather than cummingtonite because single-crystal XRD revealed an orthorhombic crystal system for this sample.

The chemical composition of samples S28 and S29 calculated from the EPMA data following the procedure recommended by IMA suggested possible C-site Li along with C-site Fe^{3+}. The presence of Li in both samples was verified by LA ICP-MS, although the measured content of Li in sample S28 was slightly less than that calculated from EPMA (see Table. 1). Overall, the chemical formulas calculated on the basis of EMPA match very well those calculated on the basis of LA ICP-MS.

Raman scattering analysis

Group-theory considerations. Amphiboles appear almost exclusively in monoclinic and orthorhombic symmetry and the most common corresponding space groups are *C*2/*m* and *Pnma* (Hawthorne and Oberti 2007). In amphiboles with space group *C*2/*m* the hydrogen atoms occupy the 4c Wyckoff position (Welch and Knight 1999) and the application of site symmetry group-theoretical analysis (Kroumova et al. 2003) reveals $2A_g+A_u+B_g+2B_u$ Raman-active phonon modes involving H vibrations. The symmetry analysis of the atomic vector displacements (Kroumova et al. 2003) shows that only one A_g mode comprises H vibrations along the ^{W}O-H bonds, i.e. consists of O-H bond stretching, and therefore only one Raman peak is expected to be seen in the range 3000-4000 cm^{-1}. Therefore multiple Raman peaks in the range of OH-bond stretching arise from the diversity in the chemical environment surrounding of OH groups. The

245 difference in the OH peak positions are caused by the difference in the O-H force
246 constants due to the impact of the adjacent atoms.

247 Similar group-theory considerations applied to monoclinic amphiboles having two
248 crystallographically distinguishable H sites in the primitive unit cell, e.g. the case of
249 cummingtonite with space group $P2_1/m$, indicate two A_g modes consisting of O-H bond
250 stretching. However according to diffraction analysis, the O-H bond lengths related to the
251 two distinguishable H atoms are the same within uncertainties (Cámara et al. 2004).
252 Therefore the corresponding phonon modes can be hardly resolved in energy and most
253 probably appear in one Raman band, if no difference exists in the chemical surrounding.
254 In the case of amphiboles with orthorhombic symmetry the allowed Raman-active O-H
255 bond stretching modes are $2A_g+2B_{2g}$ in *Pnma* and A_g+B_{1g} in *Pnnm* (Kroumova et al.
256 2003). Amphiboles with *Pnma* space group have two crystallographically distinguishable
257 H sites in the primitive unit cell but, similar to $P2_1/m$ amphiboles, the corresponding O-H
258 bond lengths are the same within uncertainties (Welch et al. 2011).

259 The fully symmetric A_g modes in all space groups typical of amphiboles usually
260 give rise to strong Raman peaks in the parallel polarized scattering geometry. Thus as a
261 Raman-spectroscopic measure of different chemical species we have used the average of
262 the integrated intensities collected in the parallel polarized spectra (the polarization of
263 incident light $\mathbf{E}_i$ is parallel to the polarization of scattered light $\mathbf{E}_s$) with the direction of
264 crystal elongation parallel or perpendicular to $\mathbf{E}_i$:
265 $[I(\text{crystal} \parallel \mathbf{E}_i \parallel \mathbf{E}_s) + I(\text{crystal} \perp \mathbf{E}_i \parallel \mathbf{E}_s)]/2$. A typical set of polarized Raman spectra
266 measured in all four scattering geometries is shown in Fig. 3.

267 **C site: M1M1M3 triplet.** There are five available C sites per formula unit (pfu),
268 consisting of two M1, two M2 and one M3 sites. The OH group shares O with a triplet of
269 $M1O_6$-$M1O_6$-$M3O_6$ octahedra (Fig. 1). Therefore the composition of the M1M1M3
270 triplet should have a huge effect on the OH bond stretching mode. Indeed, there are
271 numerous studies based on infrared spectroscopy of powdered samples (see subsection

Comparison to infrared spectroscopic studies), revealing the effect of M1 and M3 site occupancy on the position of the O-H bond stretching mode. When M1 and/or M3 sites are occupied by cations with higher electronegativity, the corresponding cation-oxygen interaction has a higher degree of covalency, which weakens the O-H bond strength and consequently, the OH-stretching peak shifts towards lower wavenumbers.

Most amphiboles contain Mg^{2+} and Fe^{2+} on the C site. The substitution of Fe^{2+} for Mg^{2+} leads to weakening of the O-H stretching force constant and therefore causes the appearance of peaks at lower wavenumbers as compared to the OH-stretching Raman peak of pure $^{C}Mg^{2+}$ amphibole (see Fig. 4). Samples with intermediate C-site composition and vacant A site may show up to four peaks in the OH stretching range related to FeFeFe, FeFeMg, FeMgMg and MgMgMg chemical configurations of the M1M1M3 triplet (Fig. 4). Note that the nomenclatures used here include all possible permutations of Mg and Fe^{2+} over the M1M1M3 triplet. Hence the content of Mg can be calculated as $Mg^{*}_{Raman} = \frac{3I_{MMM} + 2I_{FMM} + I_{FFM}}{3I_{MMM} + 3I_{FMM} + 3I_{FFM} + 3I_{FFF}}$, where I_{MMM} is the fractional intensity of the MgMgMg-OH peak (in the range of 3664 to 3674 cm^{-1} for MgMgMg-OH-$^{A}\square$ and 3715 to 3730 cm^{-1} for MgMgMg-OH-A), I_{MMF} is the fractional intensity of the MgMgFe-peak (in the range of 3643 to 3661 cm^{-1} for MgMgFe-OH-$^{A}\square$ and 3693 to 3711 cm^{-1} for MgMgFe-OH-A), I_{MFF} is the fractional intensity of the MgFeFe-peak (in the range of 3625 to 3643 cm^{-1} for MgFeFe-OH-$^{A}\square$ and 3675 to 3693 cm^{-1} for MgFeFe-OH-A), and I_{FFF} is the fractional intensity of the FeFeFe-peak (in the range of 3611 to 3625 cm^{-1} for FeFeFe-OH-$^{A}\square$ and 3661 to 3675 cm^{-1} for FeFeFe-OH-A). These spectral ranges were also conformed to previously published infrared spectroscopic data (Iezzi et al. 2004, 2005; Law and Whittaker 1981; Hawthorne and Della Ventura 2007; Robert et al. 1999; Su et al. 2009). The uncertainties in the Mg^{*}_{Raman} values were calculated from the uncertainties in the integrated intensities obtained from the fittings.

297 Since EPMA is not sensitive to the site occupancy, to quantitatively compare the
298 EPMA and Raman data we have assumed that Mg and Fe^{2+} randomly occupy all C sites
299 (M1, M2, and M3). Then the calculated amount of C-site Mg based on Raman scattering
300 Mg^*_{Raman} can be measured against that determined by EMPA
301 $Mg^*_{EMP} = \frac{^{C}Mg}{^{C}(Mg + Fe^{2+} + Li)}$, where Li is calculated as described above. Three- and
302 higher-valence cations, which have smaller ionic radii, were not taken into account since
303 these cations are expected to preferably occupy the smaller M2 site (Oberti et al. 2007;
304 Tiepolo et al. 1999) or to be associated with M1 and/or M3 sites neighboring W-site O^{2-}
305 (Hawthorne et al. 2012). If there were Al^{3+} or Fe^{3+} on M1 and/or M3 sites next to W-site
306 OH^-, their effect on the OH bond stretching would be similar to that of Fe^{2+} substituting
307 for Mg^{2+} but the associated Raman peak would appear at even lower wavenumber due to
308 the stronger influence on the O-H bond strength. This effect has been observed by
309 infrared spectroscopy in Al-rich synthetic amphiboles (Hawthorne et al. 2000). Such
310 additional peaks were not observed in the current study. Figure 5 shows Mg^*_{Raman} plotted
311 against Mg^*_{EMP}. As can be seen, there is an excellent one-to-one correlation between
312 Mg^*_{Raman} and Mg^*_{EMP}, even for samples rich in tetrahedral Al. The data points only for
313 two samples deviate from the trend, which will be discussed later (subsection **Peak**
314 **broadening and the effect of W-site F**). The relation between Mg^*_{Raman} and
315 $Mg^*_{EMP} = \frac{^{C}Mg}{^{C}(Mg + Fe^{2+})}$ is the same within uncertainties as that between Mg^*_{Raman} and
316 $Mg^*_{EMP} = \frac{^{C}Mg}{^{C}(Mg + Fe^{2+} + Li)}$ shown in Fig. 5.

317 **A site.** The A site is situated between two OH groups (Fig.1b) and hence, when
318 this site is filled, the positively charged A-site cations interact with the H^+ cations from
319 the adjacent OH groups via repulsive electrostatic forces. This leads to a confined space
320 for the motion of H^+ and restricts the freedom of the O-H bond stretching. Effectively,
321 this strengthens the O-H bonding, i.e., results in a stronger O-H force constant, and

322 therefore the corresponding Raman peak shifts towards higher wavenumber. Thus more
323 than one peak can appear also depending on the A-site occupancy. Indeed amphiboles
324 with a filled A site exhibit a broad Raman band positioned at 50-60 cm^{-1} higher than the
325 corresponding Raman peak in amphiboles with vacant A site (see Fig. 6). This result is in
326 complete agreement with previous infrared spectroscopic studies (Della Ventura et al.
327 2005; Gottschalk and Andrut 1998). Amphiboles with a partially filled A site show both
328 sharp lower-wavenumber and broad higher-wavenumber peaks, samples with completely
329 filled A site show only higher-wavenumber peaks (Fig. 6).

330 **B (M4) site.** The B site is not in the vicinity of the W site (see Fig. 1) and
331 therefore B-site cations can hardly have a strong direct effect on the O-H bond stretching
332 as M1-, M3-, and A-site cations do. However the B-site cations may have a small indirect
333 effect on the positions of the Raman peaks arising from OH bond stretching, through
334 their interactions with oxygen bridging atoms in the rings of TO_4 tetrahedra. The first
335 coordination sphere of the B site is composed of 6 oxygen atoms forming an irregular
336 octahedron plus additional oxygen atom O_{add} (marked with dashed circle in Fig. 1a)
337 positioned at a longer distance to the B site than the other six O atoms. This O_{add} atom is
338 relatively close to the adjacent OH group and can interact with H^+ via H-bonding, thus
339 weakening the O-H force constant. Assuming predominantly electrostatic (ionic)
340 interactions between the B-site cation and the O_{add} atom, B-site cations with higher
341 electrical charge or, in the case of homovalent substitution, with lower electronegativity
342 χ_p should interact stronger with O_{add}. This in turn should weaken the H-bonging between
343 O_{add} and H^+ and consequently strengthen the O-H covalent interactions, i.e., the
344 corresponding Raman peak should appear at higher wavenumbers. Indeed, the position of
345 the peak generated from the same M1M1M3-OH-$^{A}\square$ chemical species increases by ~2-3
346 cm^{-1} in the order: $^{B}Li^{+}$(χ_p=0.98) → $^{B}Na^{+}$(χ_p=0.93) → $^{B}Fe^{2+}$(χ_p=1.83) → $^{B}Mg^{2+}$
347 (χ_p=1.31) → $^{B}Ca^{2+}$(χ_p=1.00) (see Table 2).

Figure 7 shows three typical spectral changes that can be assigned to the effect of B-site cations on the OH stretching vibration. Some samples, in particular the Mg-Fe-Mn amphiboles, show subtle splitting (~3 cm^{-1}) of the peaks generated by the M1M1M3-OH-$^{A}\square$ chemical species, e.g. sample S5 shown in Fig. 7a. In general Mg and Fe^{2+} can be randomly distributed over both B and C sites but the B site exhibits tendency to accommodate more Fe^{2+} than Mg (Hitschmann et al., 1994). Following the procedure proposed by Leake et al. (2003) to calculate the chemical formula from EMPA data, S5 should contain five ^{C}Mg cations pfu and two $^{B}Fe^{2+}$ cations pfu (see Table 1). However, the presence of C-site Fe^{2+} in sample S5 is clearly revealed by the existence of three M1M1M3-OH-$^{A}\square$ Raman peaks rather than only one. This indicates that the B site as well as the C site contains both Fe^{2+} and Mg. The slight splitting of all three M1M1M3-OH-$^{A}\square$ peaks was therefore contributed to the coexistence of Fe^{2+} and Mg on the B site. The intensities of the higher- and lower-wavenumber split components are proportional to the B-site Fe^{2+} and Mg content respectively, which allows for the refinement of the B-site occupancy (see Table 1, sample S5). It is worth noting that for Mg-Fe-Mn amphiboles with chemical compositions very close to those of pure-Mg or pure-Fe^{2+} end members and having *Pnma* or $P2_1/m$ symmetry, slight splitting can occur as a pure structural effect, due to the existence of more than one Raman-active normal crystal phonon mode consisting of O-H bond stretching. In this case however, one should observe only one multi-component peak near 3669 cm^{-1} due to ^{C}(MgMgMg) -OH-$^{A}\square$ species or near 3618 cm^{-1} due to ^{C}(FeFeFe) -OH-$^{A}\square$ species. The observation of at least two peaks separated from each other by ~16 cm^{-1} indicates coexistence of Mg and Fe^{2+} on the C site, i.e. intermediate composition, and if these peaks are further split in two components by ~3 cm^{-1}, it indicates coexistence of Mg and Fe^{2+} on the B site.

Samples with B-site Na^{+} and/or Ca^{2+} show a subtle but firm decrease in the positions of the M1M1M3-OH-$^{A}\square$ peaks with Na^{+} increase and Ca^{2+} decrease (Fig.7b). The linear fit to data points for the MgMgMg-OH-$^{A}\square$ peak (the insert in Fig.7b)

375 indicates that 10% increase of B-site Na corresponds to a peak-position decrease by 0.65
376 cm^{-1}, which is accuracy achievable with modern dispersive Raman spectrometers in a lab
377 with air conditioner. Only one data point considerably deviates from the linear fit (by ~4
378 cm^{-1}), which corresponds to sample S22 rich in C-site Al (see Table 1) and will be
379 discussed in the next subsection. Samples rich in B-site Li show a pronounced shift of all
380 M1M1M3-OH-$^{A}\square$ peaks towards lower wavenumbers (see Fig. 7c). The overall
381 comparison between the available tremolite/actinolite (S7-S15) and holmquistite samples
382 (S30, 31) indicate that a total substitution of Li^{+} for Ca^{2+} on the B site should lead to a
383 decrease in the corresponding M1M1M3-OH-$^{A}\square$ peak position by ~13 cm^{-1}. This is a
384 shift two times more than the expected shift of 6.5 cm^{-1} for a total B-site substitution of
385 Na^{+} for Ca^{2+} and also exceeds a possible shift due to 100% B-site Na combined with
386 trivalent cations on the M2 site (see the next subsection). Hence a systematic shift of the
387 M1M1M3-OH-$^{A}\square$ peaks by more than 11 cm^{-1} with respect to a reference calcium-
388 amphibole sample should be indicative of Li amphiboles.

389 **C site: M2 site.** Similar to the B site, the M2 site should have none or only a
390 subtle indirect effect on the OH stretching mode (see Fig. 1). Trivalent C-site cations may
391 preferably occupy the M2 site (Oberti et al. 2007). By reason of charge neutrality
392 trivalent C-site cations are commonly present in association with univalent B-site cations.
393 Thus the shift of the M1M1M3-OH-$^{A}\square$ peak towards lower wavenumbers due to
394 univalent B-site cations (Na^{+}, Li^{+}) may be enhanced by the presence of trivalent M2-site
395 cations (Fe^{3+}, Al^{3+}).

396 In the sample suite studied here C-site Fe^{3+} with up to 0.25 site occupation factor,
397 which corresponds to approximately one M2 site pfu totally occupied by Fe^{3+}, is always
398 accompanied with high content of Na on the B site. Hence, the observed slight peak shift
399 towards lower wavenumbers can be due to B-site Na, M2-site Fe^{3+}, or combination of
400 both. According to the trend shown in the insert of Fig.7b, the observed Raman peak shift

(e.g. see Fig. 8, sample S27 versus sample S14, peak shift ~5.3 cm^{-1}) can be quantitatively explained only by the variation of ^{B}Na.

One sample (S22) with C-site occupation factor of Al equal to 0.34 shows additional shift of ~4 cm^{-1} that cannot be explained by B-site chemical variations. This extra change in the Raman peak position matches very well the observed shift of 4 cm^{-1} of the infrared OH peak induced by $^{M2}Al \rightarrow ^{M2}Mg$ in synthetic tremolite with M1 and M3 sites fully occupied by Mg (Hawthorne et al. 2000). Thus, although there were no more samples at hand with similar chemistry to draw solid conclusions about the sensitivity of Raman spectroscopy to ^{M2}Al, we assume that the effect of ^{M2}Al on the positions of Raman OH-stretching peaks is the same as the corresponding effect on the positions of the infrared OH-stretching peaks (Hawthorne et al. 2000).

Further studies on more Fe^{3+}-containg as well as Al-containing amphiboles should be performed to verify the influence of octahedrally coordinated trivalent cations on the Raman-active OH stretching modes in amphiboles.

Peak broadening and additional effects. All Raman peaks associated with OH groups next to filled A sites are much broader (FWHM ~22 ± 4 cm^{-1}) than those arising from OH groups next to vacant A sites (FWHM ~8 ± 2 cm^{-1}) (see Fig. 6). Some samples exhibit spectra with two peaks related to OH groups adjacent to occupied A sites, which are separated from each other by ~25 ± 5 cm^{-1}. In general this splitting can be due to different M1M1M3 species in the vicinity of the same A-site cation, to different A-site cations, or to different W-site anions in the vicinity of the same A-site cation. In order to figure out the origin of the splitting, we compared the spectra of two Mg-rich samples with a similar Na/K ratio on the A site, but with very different F contents (Fig. 9a). The result clearly indicates that if the A-site cation is placed between W-site F and W-site OH, the corresponding OH-stretching peak shifts towards lower wavenumbers (Fig.9a). The same phenomenon has been observed by infrared spectroscopy (Hawthorne et al. 1997; Gottschalk and Andrut 1998; Robert et al. 1999). The decrease in the peak position

can be explained by the fact that the ionic radius of F^- (r_i = 1.33 Å) is smaller than that of the hydroxyl ion (r_i = 1.37 Å). This allows the A-site cation to shift towards the F^- anion, leaving in such a way more room for the H^+ vibration, i.e. weakening the confined effect of the occupied A-site on the O-H bond stretching. The EPMA data (Table 1) indicate that the W site in sample S19 is occupied by 13% F^- and 87% OH^-, whereas sample S18 contains 58% F^- and 42 % OH^- on the W site. Therefore both OH-A-F and OH-A-OH species are possible to occur in sample S19, while predominantly OH-A-F species are expected in sample S18. Consequently, two peaks near 3710 and 3730 cm^{-1}, related to filled A sites, are observed in the spectrum of S19, while only one peak near 3705 cm^{-1} is observed for sample S18 (Fig.9a). An attempt was made to quantitatively determine the content of ^{W}F via the integrated intensities, using the relation $^{W}F_{Raman} = I_{OH\text{-}A\text{-}F}/(2I_{OH\text{-}A\text{-}F} + 2I_{OH\text{-}A\text{-}OH})$. However, good agreement between the Raman and EMPA data was achieved only for samples with negligible concentration of vacant A sites and W-site OH content larger than the F content (e.g. sample S21 in Fig.6 and sample S24 in Fig. 9b). This suggests that OH^- groups prefer to occupy W sites next to vacant A sites, while F^- anions prefer to occupy W sites next to filled A sites. Hence, the possible existence of ^{W}F-A-^{W}F, which cannot be detected by Raman spectroscopy, hinders the quantitative determination of W-site F in amphiboles.

It should be mentioned that if only the peak positions are considered as indicative of M1M1M2 species, ignoring the peak broadening due to A-site occupation as well as the influence of ^{W}F on the peak positions, one may misassign the observed OH peaks and calculate wrongly the content of Mg and Fe. For example, at the beginning of this study the two broad peaks in the spectra of samples S23 and S24, for which Mg^*_{Raman} strongly deviates from Mg^*_{EMP} (see Fig. 5), were wrongly assigned to FeMgMg and MgMgMg species (see Fig. 9b) . However, if the peak broadening is taken as an indicator of A-site occupancy, the two peaks should be attributed to two different OH-A_{filled}-W species, W =

454 OH or F. Then the two peaks can be correctly assigned to FeFeFe-OH-A-F and FeFeFe-
455 OH-A-OH and one obtains $Mg^*_{Raman} = Mg^*_{EMP} = 0$.

456 It has to be however strongly emphasized that peak broadening can also be due to
457 T-site Al (see Fig. 9c). Our data suggest that the broadening of the OH-stretching peak is
458 ~30 cm^{-1} and ~ 40 cm^{-1}, if Al occupies one and two T sites pfu, respectively. Still, the
459 FWHM of OH peaks alone cannot be used to identify ^{T}Al. For example the spectrum of
460 sample S29 contains a peak near 3700 cm^{-1} with FWHM ~ 50 cm^{-1} (see Fig. 9c), although
461 it does not contain ^{T}Al (see Table 1). The broad peak is most probably due to overlap of
462 Raman scattering signals arising from two or more different M1M1M3-OH-A-W species.
463 Preliminary results show that the strong Raman scattering near 670 cm^{-1} (see Fig.3),
464 arising from vibrations of bridging oxygen atoms in the rings of TO_4 tetrahedra
465 (Mihailova et al. 1994, 1996a), is sensitive to ^{T}Al but the comprehensive analysis of the
466 framework vibrations as well as of the effect of ^{T}Al on the OH stretching requires further
467 studies on more ^{T}Al-rich amphiboles. The results on the few ^{T}Al-rich samples considered
468 here indicate that the FWHM of the peak at 670 cm^{-1} is two to four times larger for
469 amphiboles with ^{T}Al between one to two apfu as compared to the 670-cm^{-1}-peak FWHM
470 for ^{T}Al-poor amphiboles. Tetrahedrally coordinated Al does not influence significantly
471 the positions of the peaks related to M1M1M3-OH-$^{A}\square$ species, which appear still sharp.
472 However, ^{T}Al approaching two apfu can shift the M1M1M3-OH-A_{filled}-OH peaks
473 towards lower wavenumbers by 40-45 cm^{-1}, i.e. the peaks arising from M1M1M3-OH-
474 A_{filled}-OH species in the presence of T-site Al should be positioned only at ~15-20 cm^{-1}
475 higher than the OH peaks generated by M1M1M3-OH-$^{A}\square$-OH species next to pure-Si
476 rings of TO_4 tetrahedra. Assuming that the effects of ^{W}F and ^{T}Al on the stretching of
477 ^{W}OH next to an occupied A site are additive, the positions of the broad peaks related to
478 M1M1M3-OH-A_{filled}-F in ^{T}Al-rich amphiboles is expected to be close to the positions of
479 the corresponding sharp peaks related to M1M1M3-OH-$^{A}\square$ species in the vicinity of
480 next to pure SiO_4-rings. It should be mentioned that infrared spectroscopic data on

481 synthetic ^{T}Al-rich amphiboles with entirely vacant A sites indicate considerable ^{T}Al-
482 induced broadening and downwards shift also for the M1M1M3-OH-$^{A}\square$ peaks
483 (Hawthorne et al. 2000). All ^{T}Al-rich amphiboles studied here have A-site occupation
484 factor ≥ 0.5 and the absence of any influence of ^{T}Al on the M1M1M3-OH-$^{A}\square$ Raman
485 peaks can be due to the fact that in amphiboles with partially filled A site, ^{T}Al is spatially
486 associated to filled A sites rather than to vacant A sites in order to maintain the local
487 charge balance.

488 Currently we cannot provide solid hints to distinguish between Fe^{3+} and Fe^{2+} on
489 the C site via the OH bond stretching, especially in the case of filled A site associated
490 with broad peaks. Careful examination of the framework vibrations is necessary also for
491 this purpose, which is beyond the scope of this paper.

492 **Estimation of the W-site OH content and identification of oxo-amphiboles.**
493 We have tried to find a way to quantitatively/semi-quantitatively determine the OH
494 content in amphiboles by Raman spectroscopy. For this purpose we used the ratio
495 between the sum of integrated intensities of all OH-stretching peaks and the integrated
496 intensity of the TO_4-ring peak near 670 cm^{-1}, $\eta = I_{\mathrm{OH}}^{\mathrm{total}} / I_{\mathrm{TO_4\ ring}}$. As can be seen in Fig. 10,
497 this ratio indeed steadily increases with the W-site occupancy factor of OH, suggesting
498 that for amphiboles with less than one OH pfu the ratio η should be less than 0.094. The
499 dispersion of the data points around the linear fit is relatively large, probably because the
500 sample orientation to the scattering geometry influences to a different extent the
501 components of the Raman polarizability tensors of the TO_4-ring and OH-stretching mode.

502 Sample S33 (oxo-amphibole) exhibited no measurable Raman scattering
503 generated by O-H bond stretching under the experimental conditions used. The W-site O
504 in the chemical formula can be estimated from EMPA data, following the method
505 proposed by Hawthorne et al. (2012) based on the relation between C-site Ti and the
506 chemistry on the W site. The Raman spectra of the two oxo-amphiboles (S32, S33),
507 exhibit additional Raman scattering near 750-780 cm^{-1} (see Fig. 11), which is typical of

508 TiO_6 vibrations in titanosilicates (Mihailova et al. 1996b, Kostov-Kytin et al. 2005). Due
509 to the difference in the polarizabilities of Si-O and Ti-O bonds, Ti-O vibrations can
510 produce stronger Raman scattering than Si-O vibrations (Tosheva et al. 2010). Thus the
511 extra Raman scattering at 750-780 cm^{-1} in the oxo-amphibole samples (S32, S33) might
512 be related to the relatively high amount of ^{C}Ti. The majority of oxo-amphiboles contain
513 Ti on the C site (Hawthorne et al. 2012). Hence, relatively strong Raman scattering at
514 750-780 cm^{-1} in a combination with a small ratio $\eta = I_{OH}^{total} / I_{TO_4\ ring} < 0.09$ (see Fig.10) can
515 serve as an indictor of oxo-amphiboles.

516 It is worth noting that good-quality Raman scattering of amphiboles can be
517 collected also from standard thin sections prepared for polarized light microscopy. We
518 have double checked that the Raman scattering of the resin and the glass used to prepare
519 thin sections does not contribute to the range of O-H bond stretching modes (3400 - 3800
520 cm^{-1}) and interferes only slightly with the TO_4-ring peak near 670 cm^{-1}. Therefore Raman
521 spectroscopy is applicable for crystallochemical analyses also of amphibole grains in
522 standard thin sections.

523 **Comparison to infrared spectroscopic studies.** Since the pioneering works of
524 Burns and co-workers (Burns and Strens 1966), infrared OH-stretching spectroscopy
525 carried out mainly on powdered samples has been extensively used to derive crystal-
526 chemical features of amphiboles. Our Raman spectroscopic results on the O-H bond
527 stretching modes are in good accordance with infrared spectroscopic studies by others
528 (see Table 3). The OH-stretching spectra collected by both techniques are quite similar in
529 shape and there is only a slight difference of 2-3 cm^{-1} between infrared and Raman peak
530 positions related to the same chemical species. This emphasizes the potential of Raman
531 spectroscopy to further enlarge the OH-stretching approach for even more versatile, non-
532 destructive and quick application concerning the determination of amphibole crystal-
533 chemical features.

534 **Concluding remarks: Guidelines.** Based on the suite of samples studied here,
535 we propose to use the Raman scattering from OH stretching vibrations for
536 crystallochemical analysis of amphiboles following the steps given below:
537 1. It is recommended to perform parallel polarized Raman measurements in two
538 orientations of the amphibole sample: with the direction of crystal elongation
539 perpendicular and parallel to the polarization of the incident light and then to average the
540 integrated intensities of the observed peaks. However, the consideration only of a crystal
541 orientation approximately perpendicular to the polarization of the incident light also gives
542 rather satisfactory results. To save time only the range 3400-3800 cm^{-1} is sufficient to be
543 measured; if however this spectral range is dominated by broad peaks, the spectral range
544 below 1200 cm^{-1} should be measured from the same spatial area. The recommended
545 spectral resolution is 2 cm^{-1} or better. The spectra should be fitted with pseudo-Voigt
546 functions.
547 2. Measure the Raman spectrum of a reference amphibole with known chemistry,
548 e.g. a Ca amphibole with a vacant A site (tremolite or Mg-rich actinolite), to determine
549 the MgMgMg-OH-$^{A}\square$ peak position corresponding to B-site Ca. This will be the initial
550 reference wavenumber ω_0. This value is 3672.5 cm^{-1} in our study but it may vary slightly
551 from lab to lab, depending on the protocol of spectrometer alignment.
552 3. If the spectrum contains sharp peaks (FWHM ~8 cm^{-1}), assign them to FeFeFe-
553 OH-$^{A}\square$ (~ω_0-3×16 cm^{-1}), FeFeMg-OH-$^{A}\square$ (~ω_0-2×16 cm^{-1}), FeMgMg-OH-$^{A}\square$ (~ω_0-
554 1×16 cm^{-1}), and MgMgMg-OH-$^{A}\square$ (~ω_0-0×16 cm^{-1}) species.
555 4. If the spectrum contains broad peaks with FWHM ~22 cm^{-1}: assign the peak to
556 the corresponding M1M1M3-OH-A-OH species if it is positioned at ~ω = ω(M1M1M3-
557 OH-$^{A}\square$) + 60 cm^{-1} and to the corresponding M1M1M3-OH-A-F species if it is
558 positioned at ~ω = ω(M1M1M3-OH-$^{A}\square$) + 35 cm^{-1}.

559 5. The C-site Mg* and Fe^{2+}* = 1-Mg* concentration can be calculated, using the
560 integrated peak intensities: $Mg*_{Raman} = \frac{3I_{MMM} + 2I_{FMM} + I_{FFM}}{3I_{MMM} + 3I_{FMM} + 3I_{FFM} + 3I_{FFF}}$.

561 6. If the spectrum contains sharp peaks (FWHM ~8 cm^{-1}) the predominant B site
562 chemistry can be determined: if all M1M1M3-OH-$^{A}\square$ peaks are shifted towards lower
563 wavenumbers with respect to M1M1M3-OH-$^{A}\square$ peaks of the reference Ca amphibole by
564 ~13 cm^{-1} or more, the sample is most probably Li amphibole, by ~7 cm^{-1} the sample is
565 most probably Na amphibole, by 3-5 cm^{-1} the sample can be Na-Ca amphibole with
566 $x(^{B}Na_{EMP})=(\omega_0-\omega_{sample})/6.5$ or Mg-Fe-Mn amphibole. In the case of Mg-Fe-Mn
567 amphiboles, the M1M1M3-OH-$^{A}\square$ peaks may appear split by ~3 cm^{-1} or with an
568 asymmetric shape due to the presence of weaker and stronger components and a
569 refinement of the B-site occupancy is possible, using the integrated intensities of the two
570 components.

571 7. If the OH-stretching spectral range is dominated by broad peaks with FWHM
572 ~30-40 cm^{-1} the sample may be rich in tetrahedral Al. To confirm this it is necessary to
573 check if the width of the peak near 670 cm^{-1} arising from TO_4-ring vibrations is broader
574 (two to four times) than that of the reference ^{T}Al-free amphibole sample. If this is the
575 case, the broad OH peaks arising from M1M1M3-OH-A_{filled}-OH species are expected to
576 appear at ~ω = ω(M1M1M3-OH-$^{A}\square$) + (17±5) cm^{-1} with respect to the OH peaks
577 generated by M1M1M3-OH-$^{A}\square$ species in the reference sample, while the positions of
578 the sharp peaks from M1M1M3-OH-$^{A}\square$ species as well as the positions of the broad
579 peaks from M1M1M3-OH-A_{filled}-F species are expected to be close to the positions of the
580 corresponding peaks related to M1M1M3-OH-$^{A}\square$ species in the reference sample.

581 8. If the intensity ratio between the total Raman scattering from the OH bond
582 stretching modes (3400-3800 cm^{-1}) and the Raman scattering from the bridging oxygen
583 atoms in TO_4-rings (~ 670 cm^{-1}) is less than 0.09 and a strong Raman scattering near 750-
584 780 cm^{-1} is observed, the sample should be oxo-amphibole.

IMPLICATIONS

Raman spectroscopy is becoming more and more popular among the geoscientific community because it is fast, non-destructive and can be applied to μm-sized mineral grains. There are however some skeptical viewpoints that the advantages of Raman spectroscopy are exaggerated and this method may be rather unreliable. As any experimental technique, Raman spectroscopy does have its limitations. However if the user is aware of them and conducts the Raman spectroscopic analysis carefully, this technique can be indeed very useful for "rough", certainly less precise than the common EMPA, but preparation-free and easy-to-handle crystallochemical analysis. We hope that the guidelines specified above will be helpful for non-specialists to use routinely Raman spectroscopy for identification and site-occupancy analysis of amphiboles. Also, we demonstrate that the analysis of OH stretching modes does not necessarily require the application of infrared spectroscopy and can be equally well analyzed by Raman scattering. Currently we are exploring the potential of Raman spectroscopy to be applied to another mineral supergroup of complex hydrous silicates: tourmalines.

Acknowledgements. Financial support by the Deutsche Forschungsgemeinschaft (MI 1127/7-1 and SCHL 549/6-1) is gratefully acknowledged. The authors thank Stefanie Heidrich for conducting EMP experiments, Anke Watenphul for help with LA-ICP-MS data, Thomas Malcherek for performing single-crystal XRD analysis, Joachim Ludwig for powder XRD measurements, and Peter Stutz for sample preparation for EMP and LA-ICP-MS measurements. The authors are also very grateful to the two reviewers Gianluca Iezzi and David M. Jenkins for their valuable comments and suggestions how to amend the presentation of our results.

References

612 Albrecht, M., Derrey, I. T., Horn, I., Schuth, S. Weyer, S. (2014) Quantification of trace
613 element contents in frozen fluid inclusions by UV-fs-LA-ICP-MS analysis.
614 Journal of Analytical Atomic Spectrometry, 29, 1034-1041.
615 Apopei, A. I., and Buzgar, N. (2010) The Raman study of amphiboles. Analele Ştiinţifice
616 ale Universităţii "Al. I. Cuza" Iaşi, Geologie., LVI, 57-83.
617 Bottazzi, P., Tiepolo, M., Vannucci, R., Zanetti, A., Brumm, R., Foley, S.F., and Oberti,
618 R. (1999) Contrib. Mineral. Petrol. 137, 36-45.
619 Burns R.G., and Strens R.G.J. (1966) Infrared study of the hydroxile bonds in
620 clinoamphiboles. Science 153, 890-892.
621 Cámara, F., Oberti, R., Iezzi, G., and della Ventura, G. (2003) The $P2_1/m \leftrightarrow C2/m$ phase
622 transition in synthetic amphibole $Na(NaMg)Mg_5Si_8O_{22}(OH)_2$: thermodynamic and
623 crystal-chemical evaluation. Physics and Chemistry of Minerals, 30, 570-581.
624 Chang, I. F., and Mitra, S. S. (1971) Long wavelength optical phonons in mixed crystals.
625 Advances in Physics 20, 359-404.
626 Chen, T.-H., Calligaro, T., Pagès-Camagna, S., and Menu, M. (2004) Investigation of
627 Chinese archaic jade by PIXE and μRaman spectrometry. Journal of Applied
628 Physics A, 79, 177-180.
629 Deer, W.A., Howie, R.A., and Zussman, J. (1980) An Introduction to the Rock Forming
630 Minerals, 1st ed. 12th Impression. London: Longman Group Limited.
631 Della Ventura, G., Redhammer, G. J., Iezzi, G., Hawthorne, F. C., Papin, A., and Robert,
632 J.-L. (2005) A Mössbauer and FTIR study of synthetic amphiboles along the
633 magnesioriebeckite - ferri-clinoholmquistite join. Physics and Chemistry of
634 Minerals, 32, 103-112.
635 Gottschalk, M., and Andrut M. (1998) Structural and chemical characterization of
636 synthetic (Na, K)-richterite solid solutions by EMP, HRTEM, XRD and OH-
637 valence vibrational spectroscopy. Physics and Chemistry of Minerals, 25, 101-
638 111.

639 Hawthorne, F. C., and Della Ventura, G. (2007) Short-range order in amphiboles. In
640 Hawthorne, F.C., Oberti, R., Della Ventura, G., Mottana, A., Eds., Amphiboles:
641 Crystal Chemistry, Occurrence, and Health Issues, 67, pp. 173-222, Reviews in
642 Mineralogy and Geochemistry, Mineralogical Society of America, Chantilly,
643 Virginia.
644 Hawthorne, F. C., and Oberti, R. (2007) Amphiboles: Crystal chemistry. In Hawthorne,
645 F.C., Oberti, R., Della Ventura, G., Mottana, A., Eds., Amphiboles: Crystal
646 Chemistry, Occurrence, and Health Issues, 67, pp. 1-54, Reviews in Mineralogy
647 and Geochemistry, Mineralogical Society of America, Chantilly, Virginia.
648 Hawthorne, F. C., Della Ventura, G., Robert, J.-L., Welch, M. D., Raudsepp, M., and
649 Jenkins, D. M. (1997) A Rietveld and infrared study of synthetic amphiboles
650 along the potassium-richterite-tremolite join. American Mineralogist, 82, 708-
651 716.
652 Hawthorne, F. C., Welch, M. D., Della Ventura, G., Robert, J.-L., Lui, S., and Jenkins, D.
653 M. (2000) Short-range order in synthetic aluminous tremolites: An infrared and
654 triple-quantum MAS NMR study. American Mineralogist, 85, 1716-1724.
655 Hawthorne, F. C., Oberti, R., Harlow, G., E., Maresch, W. V., Martin, R. F., Schumacher,
656 J. C., and Welch, M. D. (2012) IMA report, Nomenclature of the amphibole
657 supergroup. American Mineralogist, 97, 2031-2048.
658 Hirschmann, M., Evans, B.W., and Yang, H. (1994) Composition and temperature
659 dependence of Fe-Mg ordering incummingtonite-grunerite as determined by X-
660 ray diffraction. American Mineralogist, 79, 862-877.
661 Holland, T., and Blundy, J. (1994) Non-ideal interactions in calcic amphiboles and their
662 bearing on amphiboles-plagioclase thermometry. Contributions to Mineralogy and
663 Petrology, 116, 433-447
664 Horn, I., von Blanckenburg, F., Schoenberg R., Steinhoefel, G., and Markl, G. (2006) In
665 situ iron isotope ratio determination using UV-femtosecond laser ablation with

application to hydrothermal ore formation processes. Geochimica et Cosmochimica Acta, 70, 3677-3688.

Iezzi, G., Cámara, F., Della Ventura, G., Oberti, R., Pedrazzi, G., and Robert, J.-L. (2004) Synthesis, crystal structure and crystal chemistry of ferri-clinoholmquistite, $\square Li_2Mg_3Fe^{3+}{}_2Si_8O_{22}(OH)_2$. Physics and Chemistry of Minerals, 31, 375-385.

Iezzi, G., Della Ventura, G., Hawthorne, F. C., Pedrazzi, G., Robert, J.-L., and Novembre, D. (2005) The (Mg,Fe^{2+}) substitution in ferri-clinoholmquistite, $\square Li_2(Mg,Fe^{2+})_3Fe^{3+}{}_2Si_8O_{22}(OH)_2$. European Journal of Mineralogy, 17, 733-740.

Kloprogge, J. T., Case, M. H., and Frost, R. L. (2001) Raman microscopic study of the Li amphibole holmquistite, from the Martin Marietta Quarry, Bessemer City, NC, USA. Mineralogical Magazine, 65, 775-785.

Kostov-Kytin, V., Mihailova, B., Kalvachev, Y., and Tarassov, M. (2005) Atomic arrangements in amorphous sodium titanosilicate precursor powders. Microporous and Mesoporous Materials 86, 223-230.

Kroumova, E., Aroyo, M. I., Perez Mato, J. M., Kirov, A., Capillas, C., Ivantchev, S., and Wondratschek, H. (2003) Bilbao Crystallographic Server: useful databases and tools for phase transitions studies. Phase Transitions, 76,155-170.

Law, A. D., and Whittaker, E. J. W. (1981) Studies of the orthoamphiboles. I. The Mössbauer and infrared spectra of holmquistite. Bulletin de Minéralogie, 104, 381-386.

Leake, B. E., Woolley, A. R., Birch, W. D., Burke, E. A. J., Ferraris, G., Grice, J. D., Hawthorne, F. C., Kisch, H. J., Krivovichev, V. G., Schumacher, J. C., Stephenson, N. C. N., Whittaker, E. J. W. (2003) Nomenclature of amphiboles: additions and revisions to the International Mineralogical Association's 1997 recommendations, Canadian Mineralogist, 41, 1355-1362.

Leißner, L. (2014) Crystal chemistry of amphiboles studied by Raman spectroscopy, Master Thesis in Geoscience, University of Hamburg.

693 Martin, R. F. (2007) Amphiboles in the Igneous Enviroment. In Hawthorne, F.C., Oberti,
694 R., Della Ventura, G., Mottana, A., Eds., Amphiboles: Crystal Chemistry,
695 Occurrence, and Health Issues, 67, pp. 125-171, Reviews in Mineralogy and
696 Geochemistry, Mineralogical Society of America, Chantilly, Virginia.
697 Momma, K., and Izumi, F. (2008) VESTA: a three-dimensional visulization system for
698 electronic and structural analysis. Journal of Applied Crystallography, 41, 653-
699 658.
700 Mihailova, B., Zotov, N., Marinov, M., Nikolov, J., and Konstantinov, L. (1994)
701 Vibrational spectra of rings in silicate glasses. Journal of Non-Crystalline Solids
702 168, 265-274.
703 Mihailova, B., Gasharova, B., Konstantinov, L. (1996a): Influence of non-tetrahedral
704 cations on Si-O vibrations in complex silicates. Journal of Raman Spectroscopy
705 27, 829-833.
706 Mihailova, B., Valtchev, V., Mintova, S., and Konstantinov, L. (1996b): Vibrational
707 spectra of ETS-4 and ETS-10. Zeolites 16, 22-24.
708 Oberti, R., Hawthorne, F. C., Cannillo, E., and Cámara, F. (2007) Long-range order in
709 amphiboles. In Hawthorne, F.C., Oberti, R., Della Ventura, G., Mottana, A., Eds.,
710 Amphiboles: Crystal Chemistry, Occurrence, and Health Issues, 67, pp. 125-171,
711 Reviews in Mineralogy and Geochemistry, Mineralogical Society of America,
712 Chantilly, Virginia.
713 Oberti, R., Cannillo, E., and Toscani, G. (2012) How to name amphiboles after the
714 IMA2012 report: rules of thumb and a new PC program for monoclinic
715 amphiboles. Periodico di Mineralogia, 81, 257-267.
716 Robert, J.-L., Della Ventura, G., and Hawthorne, F. C. (1999) Near-infrared study of
717 short-range disorder of OH and F in monoclinic amphiboles. American
718 Mineralogist, 84, 86-91.

719 Su, W., Zhang, M., Redfern, S. A. T., Gao, J., and Klemd, R. (2009) OH in zoned
720 amphiboles of eclogite from the western Tianshan, NW-China. International
721 Journal of Earth Sciences, 98, 1299-1309.
722 Tiepolo, M., Zanetti, A., and Oberti, R. (1999) Detection, crystal-chemical mechanisms
723 and petrological implications of $^{[6]}Ti^{4+}$ partitioning in pargasite and kaersutite.
724 European Journal of Mineralogy, 11, 345-354.
725 Tosheva, L., Mihailova, B., Wilson, M. A., and Carter, M. A. (2010): Gravimetric study
726 of the mass gain of moisture by as fired and reheated terracotta samples. Journal
727 of the European Ceramic Society, 30, 1867-1872.
728 Vinx, R. (2008) Gesteinsbestimmung im Gelände. 2nd ed. Heidelberg: Springer
729 Spektrum.
730 Wang, A., Dhamelincourt, P., and Turrell, G. (1988) Raman and infrared spectroscopic
731 investigation of the cation distributions in amphiboles. Journal of Molecular
732 Structure, 175, 183-188.
733 Welch, M. D., and Knight, K. S. (1999) A neutron powder diffraction study of cation
734 ordering in high-temperature synthetic amphiboles. European Journal of
735 Mineralogy, 11, 321-331.
736 Welch, M. D., Cámara, F., and Oberti, R. (2011) Thermoelasticity and high-T behaviour
737 of anthophyllite, Physics and Chemistry of Minerals, 38, 321-334.
738

739

740 **Figure captions:**

741 **Figure 1**: Structure of amphibole with monoclinic (*C*2/*m*) symmetry: TO_4 tetrahedra are
742 given in dark blue; C-site chemical species are presented as olive-greenish $M1O_6$, grey
743 $M2O_6$, and light-bluish $M3O_6$ octahedra; B-site (M4) cations are given in violet; A-site
744 cations in yellow; oxygen anions in red, hydrogen cations in pink-white. The solid ellipse
745 marks a W-site OH^- group. The B-site cations can be considered to have 6 or 7 O atoms
746 in the first coordination sphere and the white dashed circles mark B-site neighboring O
747 atoms that are most distanced from the corresponding B site. The figure was prepared
748 using the VESTA software package (Momma and Izumi 2008) with the structural data by
749 Welch and Knight (1999).

750 **Figure 2**: Amphibole classification with respect to the dominant W-site and B-site
751 species (after Hawthorne *et al*., 2012); samples from the highlighted subgroups have been
752 analyzed in this study.

753 **Figure 3**: Raman spectra of Fe-containing tremolite (S11) measured in four scattering
754 geometries; crystal = direction of crystal elongation, $\mathbf{E}_i$ = polarization of incident light, $\mathbf{E}_s$
755 = polarization of scattered light. Spectra are vertically offset for clarity.

756 **Figure 4**: Raman scattering (crystal-elongation direction $\perp$ $\mathbf{E}_i$ || $\mathbf{E}_s$) of Fe-free tremolite
757 (S8) and Mg-bearing grunerite (S2), originating from OH bond stretching modes, arising
758 from different M1M1M3-OH-$^A\square$ chemical species with Mg^{2+} and Fe^{2+} randomly
759 distributed over M1 and M3.

760 **Figure 5**: Mg concentration calculated from the Raman spectroscopic data (Mg^*_{Raman})
761 versus that calculated from electron microprobe analysis (Mg^*_{EMP}). Black squares and
762 grey circles denote samples poor and rich of T-site Al, respectively. The dashed ellipse
763 marks the two samples for which Mg^*_{Raman}:Mg^*_{EMP} considerably deviates from the 1:1
764 trend, when Mg^*_{Raman} is calculated without taking into account the contribution by OH -
765 A-cation - F^- species.

766 **Figure 6**: Raman scattering (crystal-elongation direction $\perp$ $\mathbf{E}_i$ || $\mathbf{E}_s$) of tremolite (S7) and
767 richterite (S19, S21), demonstrating the effect of A-site occupancy on the OH-stretching
768 modes.
769 **Figure 7**: Raman scattering (crystal-elongation direction $\perp$ $\mathbf{E}_i$ || $\mathbf{E}_s$) generated by O-H
770 bond stretching, highlighting the effect of B-site Fe^{2+}/Mg cations (a); B-site Na (b); and
771 B-site Li (c). The inset in 7b shows the position of the MgMgMg-OH-$^{A}\square$ peak ω versus
772 the B-site occupation factor of Na determined by EMP $x(^{B}Na_{EMP})$; the line is a linear fit
773 to the majority of data points, $\omega = 3672.8 - 6.5x$.
774 **Figure 8**: Raman scattering (crystal-elongation direction $\perp$ $\mathbf{E}_i$ || $\mathbf{E}_s$) of glaucophane (S22),
775 magnesio-arfvedsonite (S27) and tremolite (S14), showing the possible effect of trivalent
776 C-site (M2-site) cations on the OH-stretching mode, in addition to the effect of univalent
777 B-site cations.
778 **Figure 9**: Raman scattering generated by O-H bond stretching (crystal-elongation
779 direction $\perp$ $\mathbf{E}_i$ || $\mathbf{E}_s$), demonstrating the effect of W-site F (a, b), possible peak
780 misassignment if the effect of F is not taken into account (b), and additional peak
781 broadening (c), which can be due to T-site Al (samples S17, S32) or overlapping of
782 Raman scattering generated by various chemical species (sample S29). Thin lines in 9b
783 and 9c represent pseudo-Voigt functions fitting the corresponding spectrum profiles.
784 **Figure 10**: Intensity ratio between the total Raman scattering generated by OH bond
785 stretching and the integrated intensity of the TO_4-ring peak near 670 cm^{-1},
786 $\eta = I_{OH}^{total} / I_{TO_4\ ring}$, versus ^{W}OH pfu calculated from EPMA. The line is a linear fit
787 $y = a + bx$ to the data points with fixed $a = 0$.
788 **Figure 11**: Raman scattering (crystal-elongation direction $\perp$ $\mathbf{E}_i$ || $\mathbf{E}_s$) of ^{T}Al-rich oxo-
789 amphiboles (kaersutite, S32 and S33) compared to the spectra of ^{T}Al-rich OH-dominant
790 amphiboles (hornblende S16 and pargasite S17). Spectra are vertically offset for clarity.
791

Table 1: Chemical composition of the studied samples calculated from EMPA with 24 anions in the chemical formula and W-site O^{2-} adjusted to the content of ^{C}Ti, following the guidelines given by Hawthorne et al. (2012). The values in the chemical formulas are rounded off to the second decimal place. The valence of Fe is 2+ if not explicitly given. The valence of Mn, Ti, and Cr is considered to be 2+, 4+, and 3+, respectively. Additional LA-ICP-MS data are included for samples S28 and S29. Site occupancy refinement after Raman data is given for sample S5. The raw EMPA data in oxide wt% are given in the supplementary table ST1.

Sample	Name (IMA2012)	$AB_2C_5T_8O_{22}W_2$				
		A	B_2 ($M4_2$)	C_5 ($M1_2M2_2M3_1$)	T_8	W_2
Mg-Fe-Mn amphiboles						
S1	anthophyllite	$□_{0.91}Na_{0.08}Ca_{0.01}$	$(Mg_{0.94}Fe_{0.06})_2$	$(Mg_{0.97}Al_{0.03})_5$	$(Al_{0.03}Si_{0.97})_8$	$OH_{2.00}$
S2	grunerite	$□_{0.97}Na_{0.01}Ca_{0.02}$	$(Fe_{0.89}Mn_{0..0}Ca_{0.01})_2$	$(Fe_{0.61}Mg_{0.39})_5$	$Si_{8.00}$	$OH_{2.00}$
S3	grunerite	$□_{0.96}Na_{0.02}Ca_{0.02}$	$(Fe_{0.75}Mn_{0.25})_2$	$(Fe_{0.71}Mg_{0.29})_5$	$Si_{8.00}$	$OH_{2.00}$
S4	cummingtonite	$□_{0.95}Na_{0.02}Ca_{0.03}$	$(Fe_{0.49}Mn_{0.45}Ca_{0.06})_2$	$(Mg_{0.66}Fe_{0.34})_5$	$(Al_{0.02}Si_{0.98})_8$	$(OH_{0.99}F_{0.005}Cl_{0.005})_2$
S5	cummingtonite	$□_{0.89}Ca_{0.07}Na_{0.03}K_{0.01}$	$(Fe_{0.98}Mn_{0.02})_2$	$Mg_{5.00}$	$(Al_{0.02}Si_{0.98})_8$	$OH_{2.00}$
Refinement after Raman data:			$(Fe_{0.62}Mg_{0.36}Mn_{0.02})_2$	$(Mg_{0.86}Fe_{0.14})_5$		
S6	cummingtonte	$□_{0.68}Na_{0.32}$	$(Mg_{0.84}Fe_{0.14}Ca_{0.02})_2$	$(Mg_{0.84}Al_{0.15}Ti_{0.01})_5$	$(Al_{0.13}Si_{0.86})_8$	$(OH_{0.99}F_{0.01})_2$
Ca amphiboles						
S7	tremolite	$□_{0.88}Na_{0.12}$	$(Ca_{0.88}Fe_{0.11}Mn_{0.01})_2$	$(Mg_{0.91}Fe_{0.08}Al_{0.01})_5$	$(Al_{0.02}Si_{0.98})_8$	$(OH_{0.99}F_{0.01})_2$
S8	tremolite	$□_{0.88}Na_{0.09}Ca_{0.03}$	$(Ca_{0.92}Mg_{0.07}Mn_{0.01})_2$	$Mg_{5.00}$	$(Al_{0.01}Si_{0.99})_8$	$(OH_{0.63}F_{0.37})_2$
S9	tremolite	$□_{0.97}Na_{0.01}Ca_{0.02}$	$(Ca_{0.94}Mg_{0.04}Mn_{0.02})_2$	$Mg_{5.00}$	$(Al_{0.01}Si_{0.99})_8$	$(OH_{0.93}F_{0.07})_2$
S10	tremolite	$□_{0.85}Na_{0.01}Ca_{0.14}$	$(Ca_{0.92}Mg_{0.06}Fe_{0.02})_2$	$Mg_{5.00}$	$(Al_{0.01}Si_{0.99})_8$	$OH_{2.00}$
S11	tremolite	$□_{0.90}Na_{0.09}K_{0.01}$	$(Ca_{0.86}Fe_{0.12}Mn_{0.02})_2$	$(Mg_{0.89}Fe_{0.10}Cr_{0.01})_5$	$(Al_{0.04}Si_{0.96})_8$	$(OH_{0.99}F_{0.01})_2$
S12	tremolite	$□_{0.92}Na_{0.07}K_{0.01}$	$(Ca_{0.90}Fe_{0.06}Mg_{0.04})_2$	$(Mg_{0.97}Al_{0.03})_5$	$(Al_{0.03}Si_{0.97})_8$	$(OH_{0.93}F_{0.07})_2$
S13	tremolite	$□_{0.95}Ca_{0.04}Na_{0.01}$	$(Ca_{0.90}Mn_{0.07}Fe_{0.03})_2$	$(Mg_{0.97}Fe_{0.03})_5$	$(Al_{0.01}Si_{0.99})_8$	$(OH_{0.87}F_{0.13})_2$
S14	tremolite	$□_{0.55}Na_{0.33}K_{0.12}$	$(Ca_{0.73}Na_{0.24}Mn_{0.04})_2$	$(Mg_{0.91}Fe_{0.08}Al_{0.01})_5$	$(Al_{0.03}Si_{0.97})_8$	$(OH_{0.86}F_{0.14})_2$
S15	actinolite	$□_{0.83}Na_{0.16}K_{0.01}$	$(Ca_{0.87}Fe_{0.12}Mn_{0.01})_2$	$(Mg_{0.86}Fe_{0.11}Al_{0.02}Cr_{0.01})_5$	$(Al_{0.02}Si_{0.98})_8$	$OH_{2.00}$
S16	magnesio-hornblende	$□_{0.51}Na_{0.45}K_{0.04}$	$(Ca_{0.87}Fe_{0.10}Mn_{0.02}Na_{0.01})_2$	$(Mg_{0.52}Fe_{0.36}Al_{0.12})_5$	$(Al_{0.14}Si_{0.86})_8$	$OH_{2.00}$
S17	pargasite	$Na_{0.63}□_{0.27}K_{0.10}$	$(Ca_{0.88}Fe_{0.10}Mn_{0.02})_2$	$(Mg_{0.41}Fe_{0.40}Al_{0.18}Ti_{0.01})_5$	$(Al_{0.22}Si_{0.78})_8$	$(OH_{0.99}F_{0.005}Cl_{0.005})_2$
S18	fluoro-edenite	$Na_{0.41}□_{0.37}K_{0.22}$	$(Ca_{0.77}Na_{0.22}Mn_{0.01})_2$	$(Mg_{0.94}Fe_{0.05}Ti_{0.01})_5$	$(Al_{0.05}Si_{0.95})_8$	$(F_{0.58}OH_{0.42})_2$

Na-Ca amphiboles						
S19	richterite	$\square_{0.47}Na_{0.32}K_{0.21}$	$(Ca_{0.64}Na_{0.27}Fe_{0.09})_2$	$(Mg_{0.94}Fe_{0.05}Al_{0.01})_5$	$Si_{8.00}$	$(OH_{0.87}F_{0.13})_2$
S20	richterite	$\square_{0.42}Na_{0.35}K_{0.23}$	$(Ca_{0.59}Na_{0.31}Fe_{0.09}Mn_{0.01}Sr_{0.01})_2$	$(Mg_{0.72}Fe_{0.26}Al_{0.01})_5$	$(Al_{0.03}Si_{0.97})_8$	$(OH_{0.93}F_{0.07})_2$
S21	richterite	$Na_{0.59}K_{0.33}\square_{0.08}$	$(Ca_{0.57}Na_{0.43})_2$	$(Mg_{0.99}Fe_{0.005}Ti_{0.005})_5$	$(Al_{0.04}Si_{0.96})_8$	$(OH_{0.76}F_{0.24})_2$
Na amphiboles						
S22	glaucophane	$\square_{0.91}Na_{0.08}K_{0.01}$	$(Na_{0.87}Ca_{0.06}Fe_{0.07})_2$	$(Mg_{0.54}Al_{0.34}Fe_{0.12})_5$	$(Al_{0.01}Si_{0.99})_8$	$(OH_{0.98}F_{0.02})_2$
S23	arfvedsonite	$Na_{0.64}K_{0.34}\square_{0.02}$	$(Na_{0.87}Ca_{0.13})_2$	$(Fe^{2+}_{0.76}Fe^{3+}_{0.19}Mg_{0.01}Mn_{0.02}Ti_{0.01})_5$	$(Al_{0.06}Si_{0.94})_8$	$(OH_{0.67}F_{0.25}O_{0.08})_2$
S24	arfvedsonite	$Na_{0.65}K_{0.36}$	$(Na_{0.78}Ca_{0.22})_2$	$(Fe^{2+}_{0.83}Fe^{3+}_{0.14}Mg_{0.03}Mn_{0.01})_5$	$(Al_{0.07}Si_{0.93})_8$	$(OH_{0.71}F_{0.26}O_{0.07})_2$
S25	arfvedsonite	$Na_{0.46}\square_{0.32}K_{0.22}$	$(Na_{0.95}Mn_{0.04}Ca_{0.01})_2$	$(Fe^{2+}_{0.73}Fe^{3+}_{0.19}Al_{0.04}Zn_{0.01}Ti_{0.01})_5$	$Si_{8.00}$	$(OH_{0.51}F_{0.45}O_{0.04})_2$
S26	magnesio-arfvedsonite	$\square_{0.48}Na_{0.35}K_{0.17}$	$(Na_{0.80}Ca_{0.15}Mn_{0.05})_2$	$(Mg_{0.72}Fe^{3+}_{0.24}Al_{0.02})_5$	$(Al_{0.02}Si_{0.98})_8$	$(OH_{0.82}F_{0.18})_2$
S27	magnesio-arfvedsonite	$\square_{0.62}Na_{0.25}K_{0.13}$	$(Na_{0.89}Ca_{0.11})_2$	$(Mg_{0.70}Fe^{3+}_{0.26}Al_{0.01}Mn_{0.01})_5$	$(Al_{0.01}Si_{0.99})_8$	$(OH_{0.85}F_{0.15})_2$
S28	ferri-fluoro-leakeite	$Na_{0.61}K_{0.42}$	$(Na_{0.95}Ca_{0.02})_2$	$(Li_{0.31}Fe^{3+}_{0.35}Mg_{0.34}Zn_{0.01})_5$	$(Al_{0.06}Si_{0.94})_8$	$(F_{0.55}OH_{0.28}O_{0.09})_2$
	LA-ICP-MS data:	$Na_{0.59}K_{0.37}\square_{0.04}$	$(Na_{0.99}Ca_{0.01})_2$	$(Li_{0.21}Fe^{3+}_{0.25}Fe^{2+}_{0.06}Mg_{0.34}Al_{0.10}Mn_{0.02}Ti_{0.01})_5$	$Si_{8.00}$	
S29	potassic-ferri-leakite	$Na_{0.52}K_{0.48}$	$(Na_{1.00})_2$	$(Mg_{0.45}Fe^{3+}_{0.31}Fe^{2+}_{0.17}Mn_{0.10}Li_{0.07}Al_{0.02}Ti_{0.02})_5$	$Si_{8.00}$	$(OH_{0.58}F_{0.34}O_{0.08})_2$
	LA-ICP-MS data:	$Na_{0.64}K_{0.30}\square_{0.06}$	$(Na_{0.98}Ca_{0.02})_2$	$(Mg_{0.36}Fe^{3+}_{0.24}Fe^{2+}_{0.20}Mn_{0.06}Al_{0.03}Li_{0.07}Ti_{0.02})_5$	$Si_{8.00}$	
Li amphiboles						
S30	clino-holmquistite	$\square_{0.98}Na_{0.02}$	$(Li_{0.98}Fe^{2+}_{0.02})_2$	$(Mg_{0.51}Al_{0.26}Fe^{2+}_{0.15}Fe^{3+}_{0.09})_5$	$(Al_{0.03}Si_{0.97})_8$	$(OH_{0.99}F_{0.01})_2$
S31	clino-ferro-holmquistite	$\square_{1.00}$	$(Li_{0.90}Na_{0.02}Fe_{0.07}Mn_{0.01})_2$	$(Al_{0.39}Fe_{0.34}Mg_{0.27})_5$	$(Al_{0.02}Si_{0.98})_8$	$OH_{2.00}$
Oxo-amphiboles						
S32	ferri-kaersutite	$Na_{0.51}K_{0.36}\square_{0.13}$	$(Ca_{0.89}Na_{0.07}Mg_{0.04})_2$	$(Mg_{0.60}Fe^{3+}_{0.21}Ti_{0.13}Al_{0.06})_5$	$(Al_{0.27}Si_{0.73})_8$	$(O_{0.65}OH_{0.32}F_{0.03})_2$
S33	kaersutite	$Na_{0.73}K_{0.18}$	$(Ca_{0.99}Mn_{0.01})_2$	$(Mg_{0.58}Ti_{0.15}Fe^{2+}_{0.15}Al_{0.02}Fe^{3+}_{0.10})_5$	$(Al_{0.27}Si_{0.73})_8$	$(O_{0.78}OH_{0.17}Cl_{0.05})_2$

Table 2: The position of the M1M1M3-OH Raman peak (in cm^{-1}) depending on chemistry as well as the peak-position differences due to different M1M1M3 chemical species ($^{M1M1M3}\Delta\omega$), dominant B-site cations ($^{B}\Delta\omega$), and OH-A-W species ($^{A\text{-}W}\Delta\omega$). Peak positions were averaged over available samples; peak positions are typed in bold while differences between wavenumber values in neighboring rows/columns are typed in italic.

	$Fe^{2+}Fe^{2+}Fe^{2+}$	$^{M1M1M3}\Delta\omega$	$Fe^{2+}Fe^{2+}Mg$	$^{M1M1M3}\Delta\omega$	$Fe^{2+}MgMg$	$^{M1M1M3}\Delta\omega$	MgMgMg	B(M4)	OH-A-W	M2
	3612	*17*	**3629**	*15.5*	**3644.5**	*15*	**3659.5**	Li	□	$Al/Mg/Fe^{2+}/Fe^{3+}$
$^{B}\Delta\omega$	*2*		*4*		*3.5*		*3.5*			
	3616	*17*	**3633**	*15*	**3648**	*14*	**3662**	Na	□	$Al/Mg/Fe^{2+}/Fe^{3+}$
$^{B}\Delta\omega$	*1*		*2*		*4*		*3*			
	3617	*18*	**3635**	*17*	**3652**	*14*	**3666**	Fe^{2+}	□	Mg/Fe^{2+}
$^{B}\Delta\omega$	*1*		*2*		*5*		*1*			
	3618	*19*	**3637**	*16*	**3653**	*14*	**3667**	Fe^{2+}/Mn^{2+}	□	Mg/Fe^{2+}
$^{B}\Delta\omega$			*2*		*2*		*2*			
	n.a.		**3639**	*16*	**3655**	*16*	**3669**	Mg	□	Mg/Fe^{2+}
$^{B}\Delta\omega$			*3*		*0*		*1*			
	3622	*19*	**3641**	*14*	**3655**	*15*	**3670**	Ca/Na	□	Mg/Fe^{2+}
$^{B}\Delta\omega$			*2*		*3*		*2.5*			
			3643	*15*	**3658**	*14.5*	**3672.5**	Ca	□	Mg/Fe^{2+}
$^{A\text{-}W}\Delta\omega$							*34.5*			
							~3707	Ca/Na	OH-Na/K-F	Mg/Fe^{2+}
$^{A\text{-}W}\Delta\omega$							*23*			
							~3730	Ca/Na	OH-Na/K-OH	Mg/Fe^{2+}

809 **Table 3**: Positions ω (in cm^{-1}) of peaks originating by OH bond stretching modes, observed in infrared (by others) and in Raman
810 spectra (this work), along with the dominant chemical elements on the non-tetrahedral sites.
811

$\omega_{Infrared}$	A	M4	M1M1M3	M2	W	Reference	ω_{Raman}	A	M4	M1M1M3	M2	W	Sample
3614	□	Li	$Fe^{2+}Fe^{2+}Fe^{2+}$	Fe^{3+}	OH	Iezzi et al. (2005, 2004), Kloprogge 2001	3611	□	Li	$Fe^{2+}Fe^{2+}Fe^{2+}$	Al/Fe^{3+}	OH	S31
3618	□	n.a.	$Fe^{2+}Fe^{2+}Al$	n.a.	OH	Law and Whittaker (1981)	3617	□	Fe^{2+}	$Fe^{2+}Fe^{2+}Fe^{2+}$	Mg/Fe^{2+}	OH	S2
							3618	□	Fe^{2+}/Mn	$Fe^{2+}Fe^{2+}Fe^{2+}$	Mg/Fe^{2+}	OH	S3, S4
3626	□	Ca	$Fe^{2+}Fe^{2+}Fe^{2+}$	Fe^{2+}/Mg	OH	Chen et al (2004)							
3631	□	Li	$MgFe^{2+}Fe^{2+}$	Fe^{3+}	OH	Iezzi et al. (2005, 2004), Kloprogge (2001)	3629.5	□	Li	$MgFe^{2+}Fe^{2+}$	Al	OH	S30
3634	□	Na	$MgFe^{2+}Fe^{2}$	Al	OH	Su et al. (2009), Kloprogge	3633	□	Na	$MgFe^{2+}Fe^{2+}$	Al	OH	S22
3634	□	n.a	$MgFe^{2+}Al$	n.a.	OH	Law and Whittaker (1981)	3635	□	Fe^{2+}	$MgFe^{2+}Fe^{2+}$	Mg/Fe^{2+}	OH	S2, S5
							3637	□	Fe^{2+}/Mn	$MgFe^{2+}Fe^{2+}$	Mg/Fe^{2+}	OH	S3, S4
							3639	□	Mg	$MgFe^{2+}Fe^{2+}$	Mg/Fe^{2+}	OH	S5
3645	□	Ca	$MgFe^{2+}Fe^{2+}$	Fe^{2+}/Mg	OH	Chen et al. (2004)	3644	□	Ca	$MgFe^{2+}Fe^{2+}$	Mg/Fe^{2+}	OH	S15
3647	□	Li	$MgMgFe^{2+}$	Fe^{3+}	OH	Iezzi et al. (2005, 2004), Kloprogge (2001)	3646	□	Li	$MgMgFe^{2+}$	Al	OH	S30
3646-3649	□	Na	$MgMgFe^{2+}$	n.a.	OH	Su et al. (2009)	3648	□	Na	$MgMgFe^{2+}$	Al	OH	S22
3651	□	n.a.	MgMgAl	n.a.	OH	Law and Whittaker (1981)	3651-3652	□	Fe	$MgMgFe^{2+}$	Mg/Fe^{2+}	OH	S2, S3
							3653	□	Fe^{2+}/Mn	$MgMgFe^{2+}$	Mg/Fe^{2+}	OH	S3, S4
3658-3660	□	Na	MgMgMg	Al	OH	Su et al. (2009)	3655	□	Mg	$MgMgFe^{2+}$	Mg/Fe^{2+}	OH	S5
3661	□	Ca	$MgMgFe^{2+}$	Fe^{2+}/Mg	OH	Chen et al. (2004)	3659	□	Ca	$MgMgFe^{2+}$	Mg/Fe^{2+}	OH	S7, S11, S15
3662	□	Li	$MgMgFe^{2+}$	Fe^{3+}	OH	Iezzi et al. (2005, 2004), Kloprogge (2001)	3659.5	□	Li	MgMgMg	Al	OH	S30
							3661	□	Na	MgMgMg	Al	OH	S22

3668	□	Mg, Fe^{2+}	MgMgMg	Fe^{2+}/Mg	OH	Iezzi (2004)	3664	□	Na	MgMgMg	Al	OH	S14
							3666	□	Na/Ca	MgMgMg	Mg/Fe^{2+}	OH	S27
							3667	□	Fe^{2+}	MgMgMg	Mg/Fe^{2+}	OH	S5, S11
3670	□	Mg	MgMgMg	Mg	OH	Hawthorne et al. (1997)	3669.5	□	Mg	MgMgMg	Mg/Fe^{2+}	OH	S5
3674	□	Mg	MgMgMg	Fe^{2+}/Mg	OH	Chen et al. (2004)							
3675	□	Ca	MgMgMg	Fe^{2+}/Mg	OH	Iezzi (2004), Chen et al. (2004)	3672-3673	□	Ca	MgMgMg	Mg	OH	S7, S8, S10-S16, S18, S32
3693	Li	n.a.	MgMgFe^{2+}	Fe^{2+}/Mg	OH	Iezzi (2004)							
3709	Li	n.a.	MgMgMg	Fe^{2+}/Mg	OH	Iezzi (2004)							
3711	Na	Ca	MgMgMg	Mg	F, OH	Robert et al. (1999)	~3707	Na/K	Ca/Na	MgMgMg	Mg/Fe^{2+}	F,OH	S6, S19
3714	K	Ca	MgMgMg	Mg	F, OH	Robert et al. (1999)							
3730	Na	Ca	MgMgMg	Mg	OH	Robert et al. (1999)	~3730	Na/K	Ca/Na	MgMgMg	Mg/Fe^{2+}	OH	S19
3734	K	Ca	MgMgMg	Ca	OH	Hawthorne et al. (1997), Hawthorne and Della Ventura (2007)							

812

813

Supplementary Table ST1. Mean values and standard deviations of metal oxides, F, and Cl (wt%) measured by EMPA; b.d.l. stands for "below the detection limit".

Sample	SiO_2	TiO_2	Al_2O_3	Cr_2O_3	FeO	MgO	MnO	CaO	Na_2O	K_2O	ZnO	SrO	BaO	F	Cl	Total
S1	58.64 ± 0.27	0.07 ± 0.02	2.79 ± 0.27	0.01 ± 0.01	1.03 ± 0.07	34.17 ± 0.26	b.d.l.	0.18 ± 0.02	0.30 ± 0.06	0.01 ± 0.01	0.01 ± 0.02	0.06 ± 0.12	b.d.l.	0.01 ± 0.01	0.020 ± 0.005	97.3 ± 0.4
S2	50.2 ± 0.9	0.01 ± 0.01	0.25 ± 0.05	0.01 ± 0.01	36.2 ± 1.5	8.3 ± 0.8	1.43 ± 0.22	0.24 ± 0.04	0.02 ± 0.03	0.01 ± 0.00	0.08 ± 0.04	0.06 ± 0.08	0.03 ± 0.01	0.06 ± 0.03	b.d.l.	96.9 ± 0.7
S3	48.95 ± 0.17	0.02 ± 0.01	0.17 ± 0.05	0.01 ± 0.01	37.39 ± 0.24	5.95 ± 0.06	3.63 ± 0.04	0.11 ± 0.01	0.01 ± 0.01	0.11 ± 0.06	0.01 ± 0.02	0.01 ± 0.03	0.05 ± 0.08	0.00 ± 0.00	0.02 ± 0.03	96.43 ± 0.23
S4	52.33 ± 0.41	0.03 ± 0.02	0.77 ± 0.12	b.d.l.	21.3 ± 1.4	14.5 ± 1.0	7.00 ± 0.20	1.03 ± 0.24	0.08 ± 0.01	0.02 ± 0.04	0.06 ± 0.03	0.1 ± 0.3	b.d.l.	0.01 ± 0.03	0.030 ± 0.005	97.2 ± 0.4
S5	54.67 ± 0.36	0.05 ± 0.07	0.52 ± 0.25	0.03 ± 0.01	16.30 ± 0.22	23.53 ± 0.14	0.32 ± 0.41	0.44 ± 0.03	0.09 ± 0.02	0.06 ± 0.15	0.03 ± 0.02	0.03 ± 0.04	0.02 ± 0.02	0.02 ± 0.02	b.d.l.	96.1 ± 0.5
S6	51.23 ± 0.05	0.19 ± 0.02	12.0 ± 0.6	0.01 ± 0.01	2.50 ± 0.18	29.5 ± 0.3	0.00 ± 0.01	0.19 ± 0.01	1.25 ± 0.04	0.01 ± 0.02	0.02 ± 0.03	b.d.l.	0.01 ± 0.03	0.05 ± 0.03	0.030 ± 0.005	96.9 ± 0.6
S7	55.68 ± 0.25	0.03 ± 0.01	1.33 ± 0.17	0.33 ± 0.12	4.82 ± 0.19	21.62 ± 0.25	0.22 ± 0.02	11.35 ± 0.11	0.45 ± 0.08	0.05 ± 0.01	0.02 ± 0.02	0.02 ± 0.04	b.d.l.	0.04 ± 0.04	b.d.l.	95.96 ± 0.23
S8	57.12 ± 0.29	0.02 ± 0.02	0.53 ± 0.10	0.01 ± 0.01	0.08 ± 0.03	24.91 ± 0.15	0.03 ± 0.14	12.57 ± 0.22	0.34 ± 0.05	0.05 ± 0.01	0.02 ± 0.02	0.08 ± 0.19	b.d.l.	1.72 ± 0.08	0.010 ± 0.005	97.5 ± 0.5
S9	57.96 ± 0.24	0.15 ± 0.01	0.29 ± 0.09	0.01 ± 0.01	0.15 ± 0.04	24.81 ± 0.11	0.07 ± 0.38	12.91 ± 0.13	0.03 ± 0.01	0.02 ± 0.01	0.02 ± 0.02	0.06 ± 0.15	b.d.l.	0.34 ± 0.04	b.d.l.	96.7 ± 0.6
S10	57.35 ± 0.3	0.01 ± 0.01	0.17 ± 0.02	b.d.l.	0.45 ± 0.04	24.87 ± 0.14	0.01 ± 0.01	13.30 ± 0.07	0.03 ± 0.01	0.01 ± 0.01	0.01 ± 0.02	b.d.l.	b.d.l.	0.02 ± 0.03	0.020 ± 0.005	96.2 ± 0.5
S11	55.1 ± 0.4	0.05 ± 0.01	2.24 ± 0.30	0.26 ± 0.15	4.08 ± 0.14	21.61 ±0.26	0.19 ± 0.02	11.37 ± 0.09	0.34 ± 0.05	0.04 ± 0.01	0.01 ± 0.02	0.06 ± 0.11	b.d.l.	0.05 ± 0.03	b.d.l.	95.4 ± 0.3
S12	56.2 ± 0.5	0.03 ± 0.02	2.4 ± 0.5	0.00 ± 0.01	0.96 ± 0.10	23.9 ± 0.5	0.01 ± 0.01	12.2 ± 0.4	0.25 ± 0.07	0.03 ± 0.01	0.02 ± 0.02	0.01 ± 0.02	b.d.l.	0.30 ± 0.05	b.d.l.	96.3 ± 0.5
S13	57.8 ± 0.3	0.02 ± 0.01	0.16 ± 0.04	0.01 ± 0.01	1.69 ± 0.21	23.85 ± 0.27	1.19 ± 0.11	12.60 ± 0.3	0.03 ± 0.01	0.03 ± 0.05	0.03 ± 0.02	b.d.l.	b.d.l.	0.61 ± 0.06	b.d.l.	98.0 ± 0.5
S14	55.55 ± 0.21	0.03 ± 0.01	2.12 ± 0.08	0.01 ± 0.01	3.31 ± 0.10	21.99 ± 0.09	0.61 ± 0.04	9.72 ± 0.12	2.96 ± 0.04	0.66 ± 0.09	0.03 ± 0.03	0.01 ± 0.01	0.01 ± 0.02	0.64 ± 0.05	0.01 ± 0.05	97.67 ± 0.28
S15	55.04 ± 0.25	0.02 ± 0.01	1.68 ± 0.08	0.42 ± 0.06	6.46 ± 0.14	20.45 ± 0.15	0.16 ± 0.02	11.01 ± 0.09	0.59 ± 0.02	0.04 ± 0.01	0.02 ± 0.02	0.01 ± 0.01	b.d.l.	0.02 ± 0.02	b.d.l.	95.9 ± 0.3
S16	46.3 ± 0.8	0.21 ± 0.02	9.5 ± 0.8	0.00 ± 0.01	15.8 ± 0.3	11.8 ± 0.5	0.26 ± 0.02	10.90 ± 0.12	1.62 ± 0.11	0.21 ± 0.03	0.03 ± 0.02	b.d.l.	b.d.l.	0.02 ± 0.03	b.d.l.	96.7 ± 0.3
S17	41.2 ± 0.4	0.39 ± 0.02	14.7 ± 0.4	0.02 ± 0.02	17.37 ± 0.21	9.08 ± 0.18	0.28 ± 0.03	10.75 ± 0.10	0.03 ± 0.04	0.46 ± 0.03	0.03 ± 0.03	0.00 ± 0.00	b.d.l.	0.03 ± 0.01	0.03 ± 0.01	96.50 ± 0.23
S18	55.2 ±	0.07 ±	1.76 ±	0.01 ±	2.02 ±	23.01	0.16 ±	10.49	3.20 ±	1.25 ±	0.04 ±	0.02 ±	0.010	2.66 ±	0.01 ±	99.9 ± 0.5

S19	0.3 56.4 ± 0.3	0.01 0.04 ± 0.01	0.04 0.26 ±0.04	0.01 0.01 ± 0.01	0.05 3.65 ± 0.19	± 0.15 22.35 ± 0.17	0.02 0.09 ± 0.33	± 0.06 8.39 ± 0.16	0.03 3.16 ± 0.11	0.07 1.18 ± 0.07	0.03 0.03 ± 0.02	0.06 0.07 ±0.19	± 0.05 b.d.l.	0.10 0.61 ± 0.06	0.01 b.d.l.	96.2 ± 0.5
S20	53.17 ± 0.78	0.21 ± 0.07	1.71 ± 0.35	0.01 ± 0.01	11.87 ± 1.12	16.62 ± 0.80	0.20 ± 0.02	7.5 ± 1.1	3.40 ± 0.60	1.2 ± 0.3	0.02 ± 0.02	0.2 ± 0.5	0.05 ± 0.14	0.32 ± 0.05	0.01 ± 0.02	96.51 ± 0.5
S21	55.86 ± 0.27	0.12 ± 0.01	1.72 ± 0.10	0.00 ± 0.01	0.09 ± 0.03	24.05 ± 0.10	0.04 ± 0.01	7.75 ± 0.08	5.43 ± 0.05	1.87 ± 0.02	0.01 ± 0.02	0.01 ± 0.01	b.d.l.	1.12 ± 0.06	0.02 ± 0.03	98.1 ± 0.3
S22	57.74 ± 0.28	0.04 ± 0.02	10.76 ± 0.28	0.31 ± 0.10	6.28 ± 0.27	13.14 ± 0.28	0.07 ± 0.06	0.75 ± 0.19	6.82 ± 0.12	0.03 ± 0.02	0.03 ± 0.02	0.06 ± 0.08	0.02 ± 0.02	0.08 ± 0.03	b.d.l.	96.14 ± 0.28
S23	46.04 ± 0.18	0.61 ± 0.05	2.59 ± 0.37	0.01 ± 0.01	34.6 ± 0.6	0.17 ± 0.02	0.59 ± 0.07	1.48 ± 0.09	7.53 ± 0.19	1.64 ± 0.15	0.11 ± 0.04	b.d.l.	b.d.l.	0.99 ± 0.10	b.d.l.	96.4 ± 0.6
S24	45.62 ± 0.30	0.59 ± 0.02	2.63 ± 0.04	b.d.l.	35.45 ± 0.25	0.12 ± 0.01	0.56 ± 0.02	2.49 ± 0.03	6.93 ± 0.08	1.74 ± 0.01	0.10 ± 0.04	b.d.l.	b.d.l.	1.01 ± 0.07	b.d.l.	97.2 ± 0.5
S25	49.74 ± 0.33	0.30 ± 0.02	1.07 ± 0.04	b.d.l.	34.19 ± 0.23	0.04 ± 0.01	1.24 ± 0.06	0.14 ± 0.12	7.57 ± 0.18	1.05 ± 0.06	0.48 ± 0.04	b.d.l.	0.01 ± 0.02	1.76 ± 0.11	b.d.l.	97.6 ± 0.5
S26	55.94 ± 0.26	0.09 ± 0.01	1.07 ± 0.10	0.01 ±0.01	10.39 ± 0.23	17.41 ± 0.16	0.76 ± 0.09	2.04 ± 0.08	7.24 ± 0.10	0.95 ± 0.19	0.03 ± 0.02	0.04 ± 0.07	0.02 ± 0.05	0.82 ± 0.06	b.d.l.	96.8 ± 0.4
S27	56.64 ± 0.29	0.02 ± 0.01	0.61 ± 0.04	0.01 ± 0.01	11.1 ± 0.5	16.76 ± 0.76	0.45 ± 0.07	1.55 ± 0.13	7.41 ± 0.13	0.71 ± 0.08	0.02 ± 0.02	b.d.l.	b.d.l.	0.68 ± 0.07	0.01 ± 0.01	96.0 ± 0.4
S28	54.48 ± 0.68	0.9 ± 0.6	2.10 ± 0.71	0.02 ± 0.01	15.27 ± 2.36	8.10 ± 1.71	0.73 ± 0.12	0.19 ± 0.21	9.28 ± 0.80	2.4 ± 0.6	0.48 ± 0.08	b.d.l.	0.01 ± 0.01	2.50 ± 0.66	b.d.l.	96.5 ± 0.5
S29	54.63 ± 0.19	0.73 ± 0.08	0.56 ± 0.05	b.d.l.	13.82 ± 0.17	10.22 ± 0.08	3.98 ± 0.13	0.06 ± 0.01	8.90 ± 0.07	2.69 ± 0.08	0.09 ± 0.04	0.02 ± 0.02	b.d.l.	1.53 ± 0.09	b.d.l.	97.3 ± 0.4
S30	60.83 ± 0.32	0.01 ± 0.01	8.35 ± 0.25	0.01 ± 0.01	10.9 ± 0.3	13.00 ± 0.12	0.19 ± 0.02	0.02 ± 0.01	0.08 ± 0.01	0.01 ± 0.03	0.09 ± 0.03	b.d.l.	b.d.l.	0.06 ± 0.04	b.d.l.	93.6 ± 0.4
S31	58.11 ± 1.11	0.03 ± 0.02	13.02 ± 0.41	0.01 ± 0.01	15.9 ± 0.5	6.58 ± 0.19	0.15 ± 0.03	0.02 ± 0.01	0.16 ± 0.04	b.d.l.	0.04 ± 0.03	b.d.l.	b.d.l.	0.01 ± 0.02	b.d.l.	94.0 ± 0.6
S32	39.45 ± 0.28	5.91 ± 0.03	14.09 ± 0.09	0.03 ± 0.02	8.29 ± 0.13	13.93 ± 0.15	0.09 ± 0.02	11.12 ± 0.07	2.26 ± 0.03	1.93 ± 0.01	0.03 ± 0.02	0.04 ± 0.03	0.16 ± 0.02	0.13 ± 0.05	0.010 ± 0.005	97.5 ± 0.5
S33	38.62 ± 0.16	6.75 ± 0.14	12.68 ± 0.13	0.01 ± 0.01	9.7 ± 0.4	13.20 ± 0.16	0.12 ± 0.02	12.18 ± 0.07	2.49 ± 0.03	0.93 ± 0.02	0.03 ± 0.03	0.07 ± 0.04	0.24 ± 0.04	0.30 ± 0.05	b.d.l.	97.4 ±0.4

819

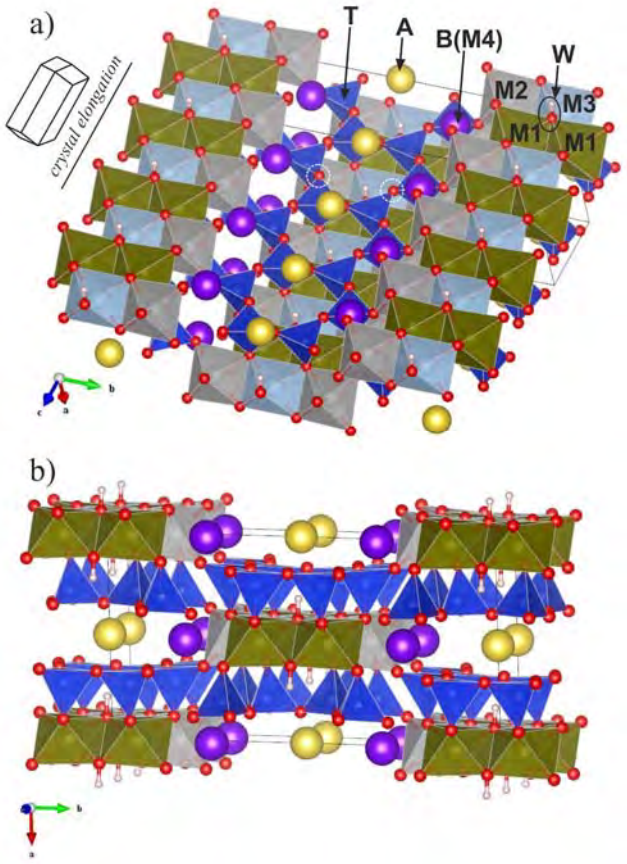

820

821

822 **Figure 1**

823

824

825

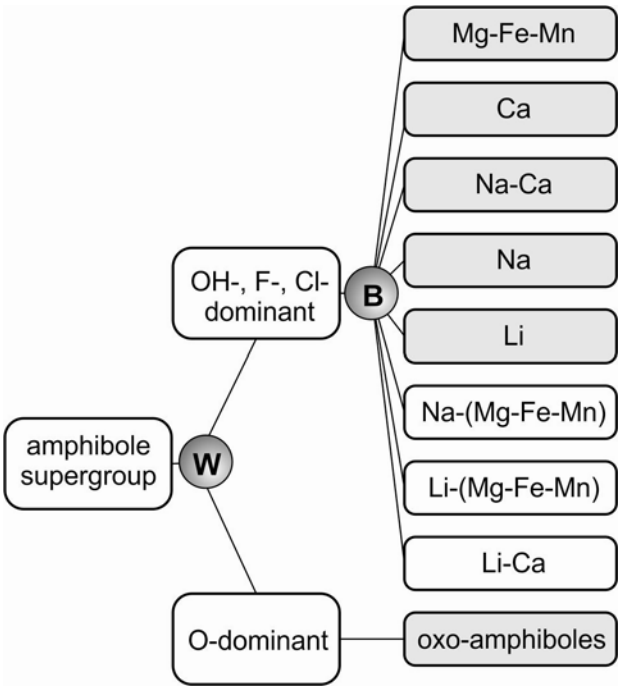

826

827

828 **Figure 2**

829

830

831

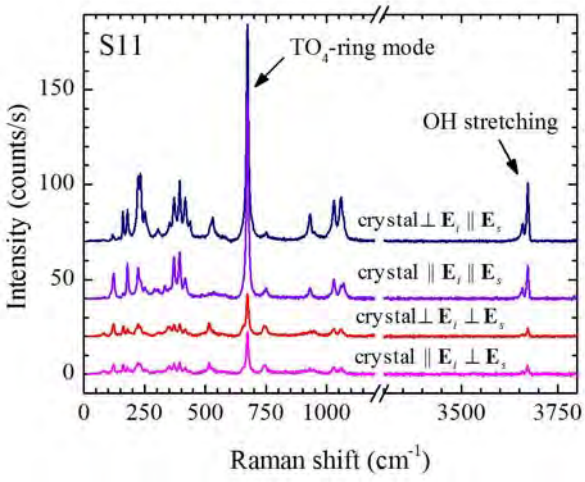

832

833

834 **Figure 3**

835

836

837

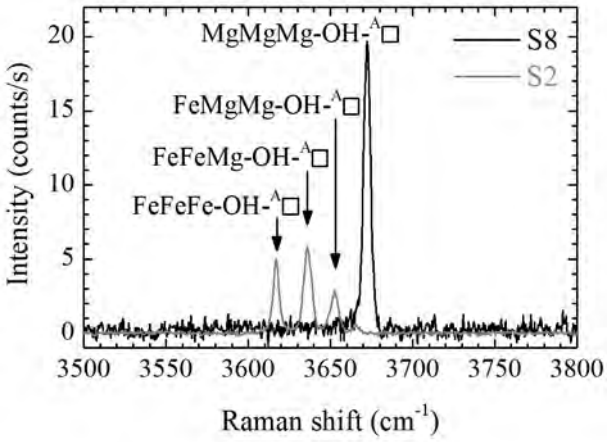

838

839

840 **Figure 4**

841

842

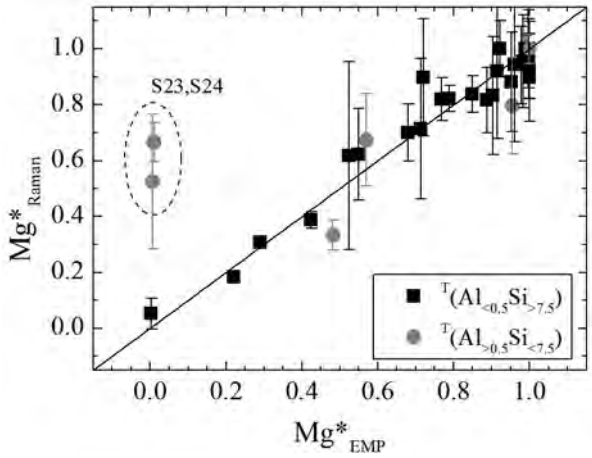
S23,S24
Mg*Raman
Mg*EMP
1.0
0.8
0.6
0.4
0.2
0.0
0.0
0.2
0.4
0.6
0.8
1.0
T(Al<0.5Si>7.5)
T(Al>0.5Si<7.5)

Figure 5

849

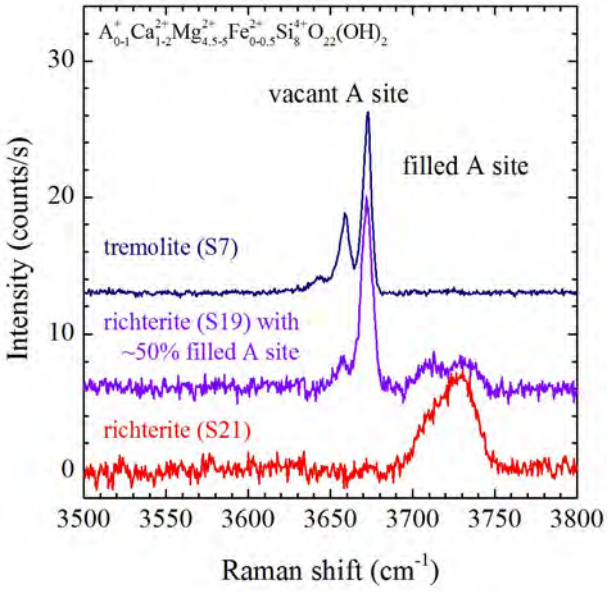

850

851

852 **Figure 6**

853

854

855

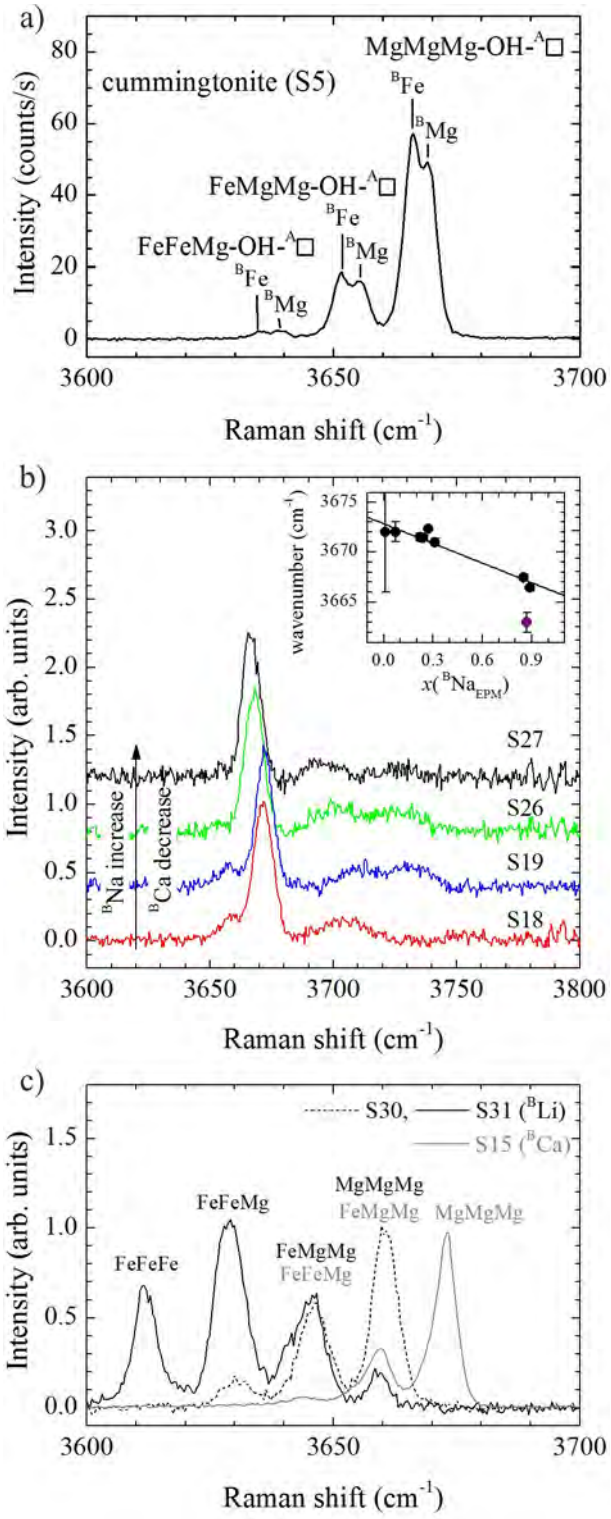

856

857

858 **Figure 7**

859

860

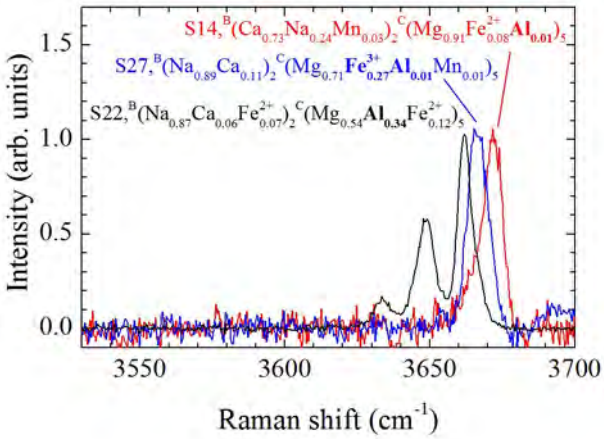

861

862

863 **Figure 8**

864

865

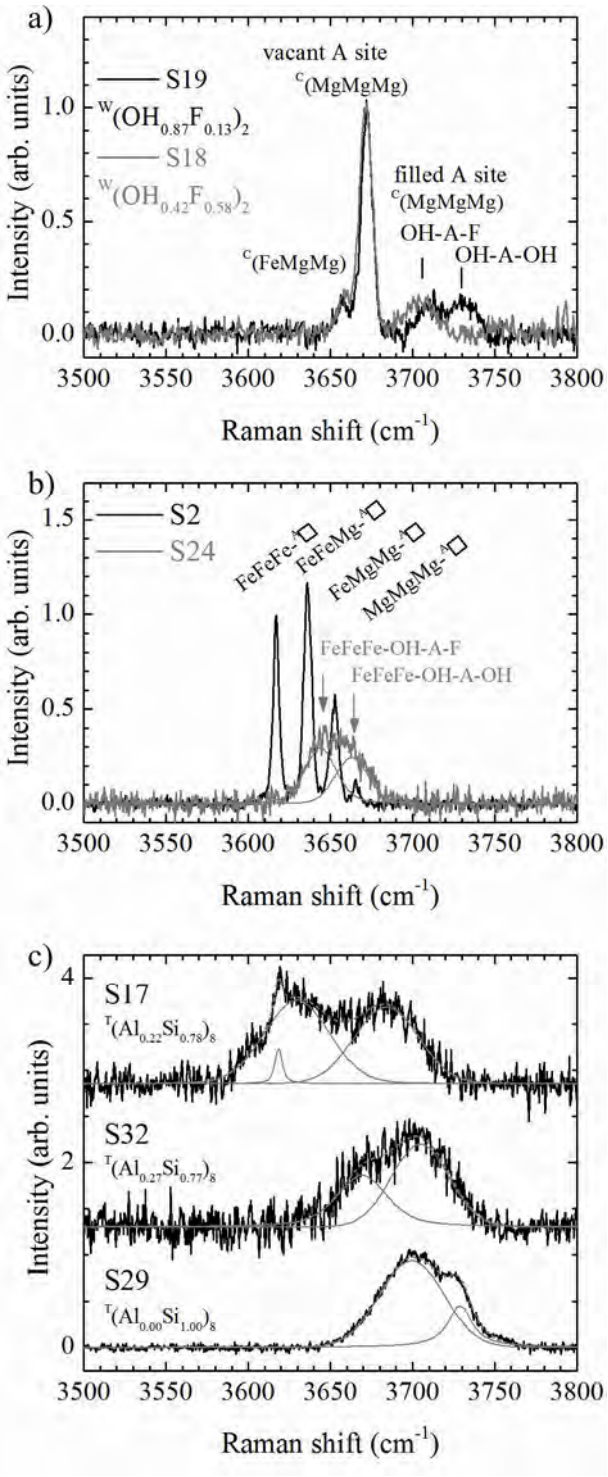
a)
vacant A site
S19
W(OH0.87F0.13)2
S18
W(OH0.42F0.58)2
C(MgMgMg)
filled A site
C(MgMgMg)
OH-A-F
OH-A-OH
C(FeMgMg)
Intensity (arb. units)
Raman shift (cm-1)
b)
S2
S24
FeFeFe-A□
FeFeMg-A□
FeMgMg-A□
MgMgMg-A□
FeFeFe-OH-A-F
FeFeFe-OH-A-OH
Intensity (arb. units)
Raman shift (cm-1)
c)
S17
T(Al0.22Si0.78)8
S32
T(Al0.27Si0.77)8
S29
T(Al0.00Si1.00)8
Intensity (arb. units)
Raman shift (cm-1)

Figure 9

872

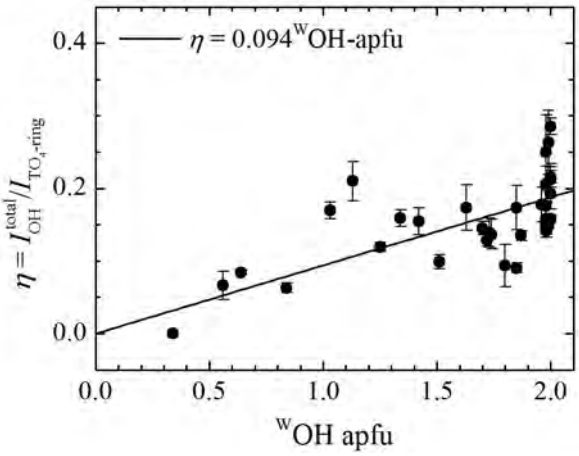

873

874

875 **Figure 10**

876

877

878

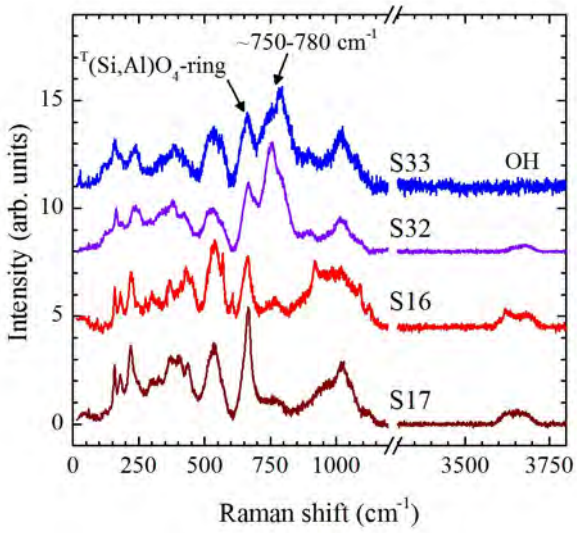

879

880

881 **Figure 11**

882

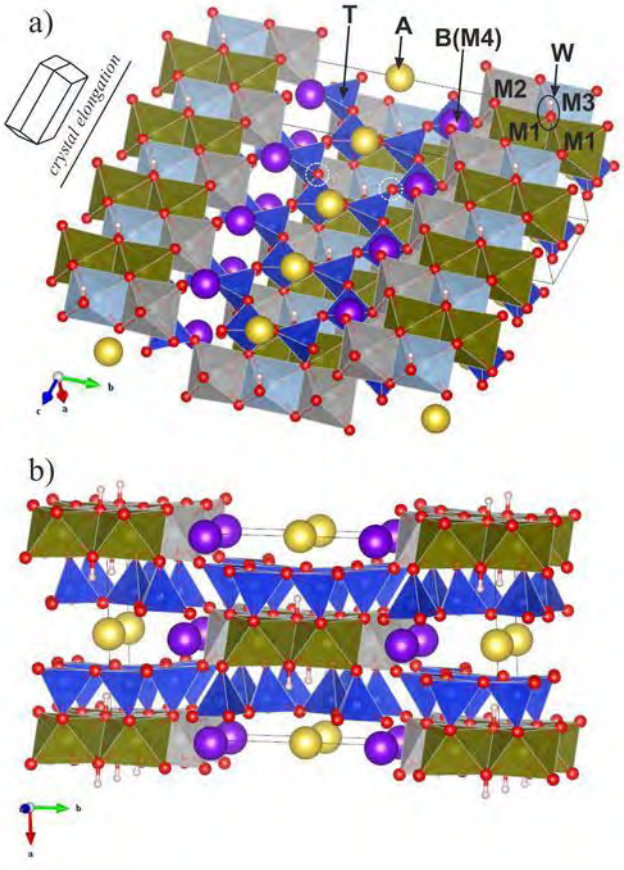
a)
crystal elongation
T
A
B(M4)
W
M2
M3
M1
M1
b)

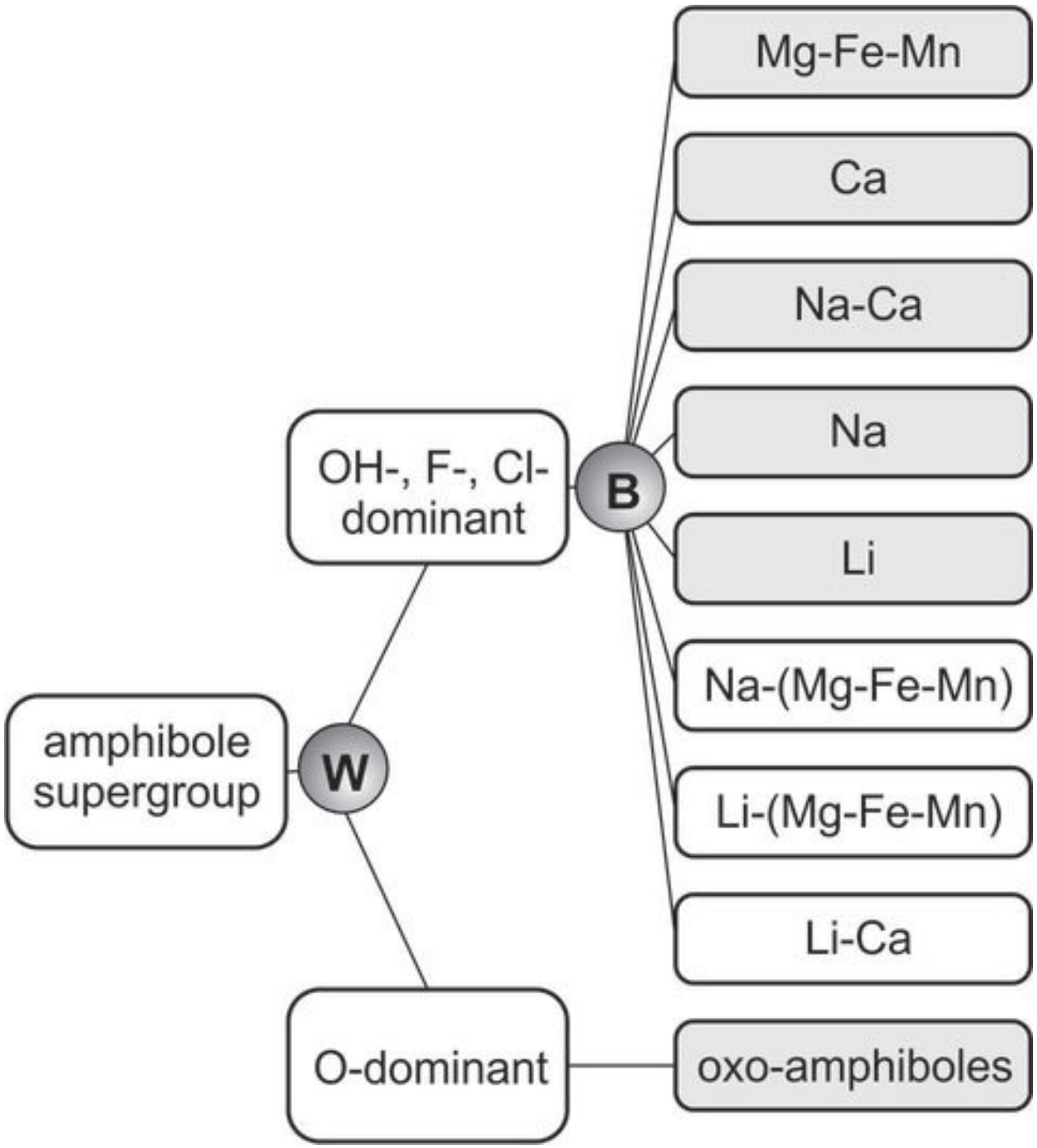
amphibole supergroup
W
OH-, F-, Cl-dominant
B
Mg-Fe-Mn
Ca
Na-Ca
Na
Li
Na-(Mg-Fe-Mn)
Li-(Mg-Fe-Mn)
Li-Ca
O-dominant
oxo-amphiboles

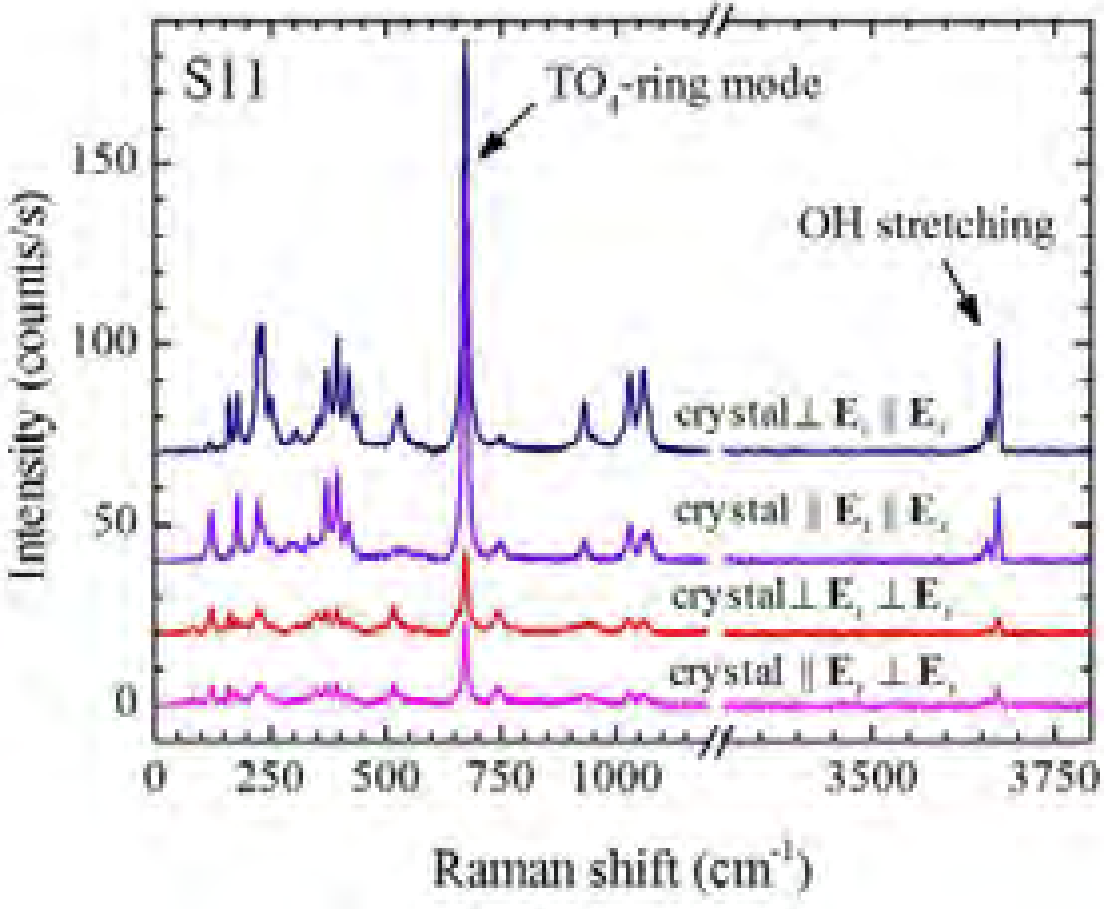
S11
TO4-ring mode
OH stretching
crystal⊥ E1 ∥ E2
crystal ∥ E1 ∥ E2
crystal⊥ E1 ⊥ E2
crystal ∥ E1 ⊥ E2
Intensity (counts/s)
150
100
50
0
0
250
500
750
1000
3500
3750
Raman shift (cm-1)

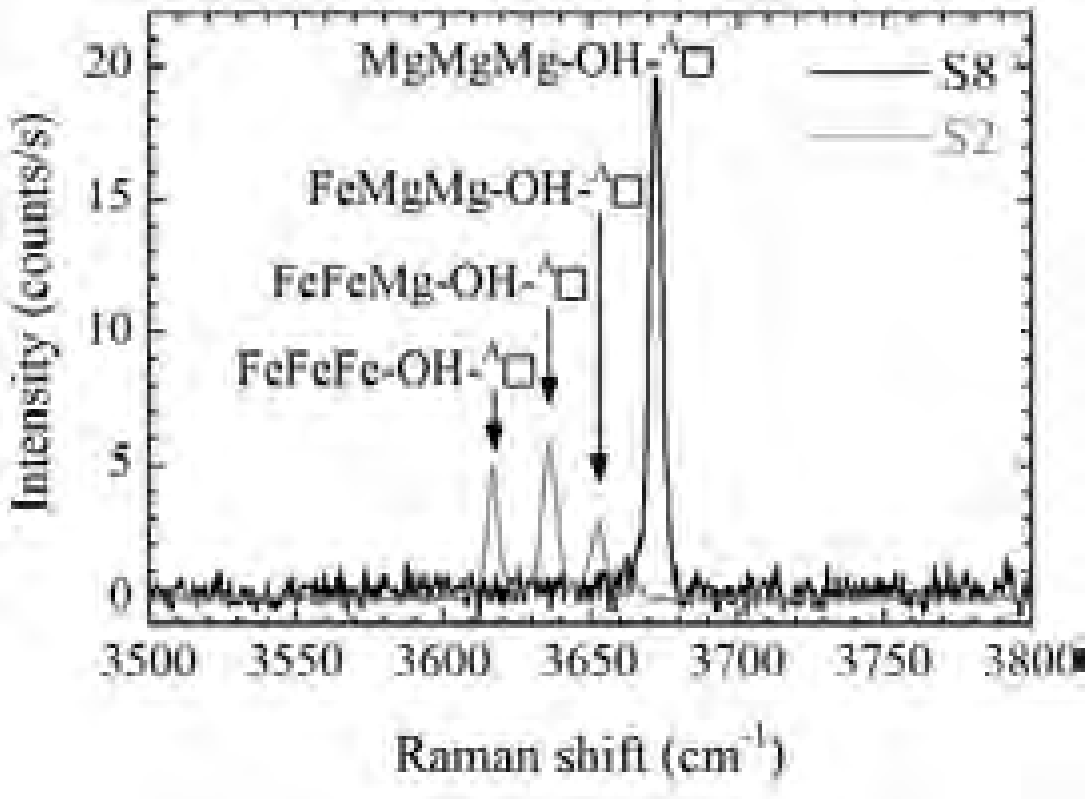
MgMgMg-OH-^{A}□
FeMgMg-OH-^{A}□
FeFeMg-OH-^{A}□
FeFeFe-OH-^{A}□
S8
S2
Intensity (counts/s)
Raman shift (cm^{-1})
0
5
10
15
20
3500
3550
3600
3650
3700
3750
3800

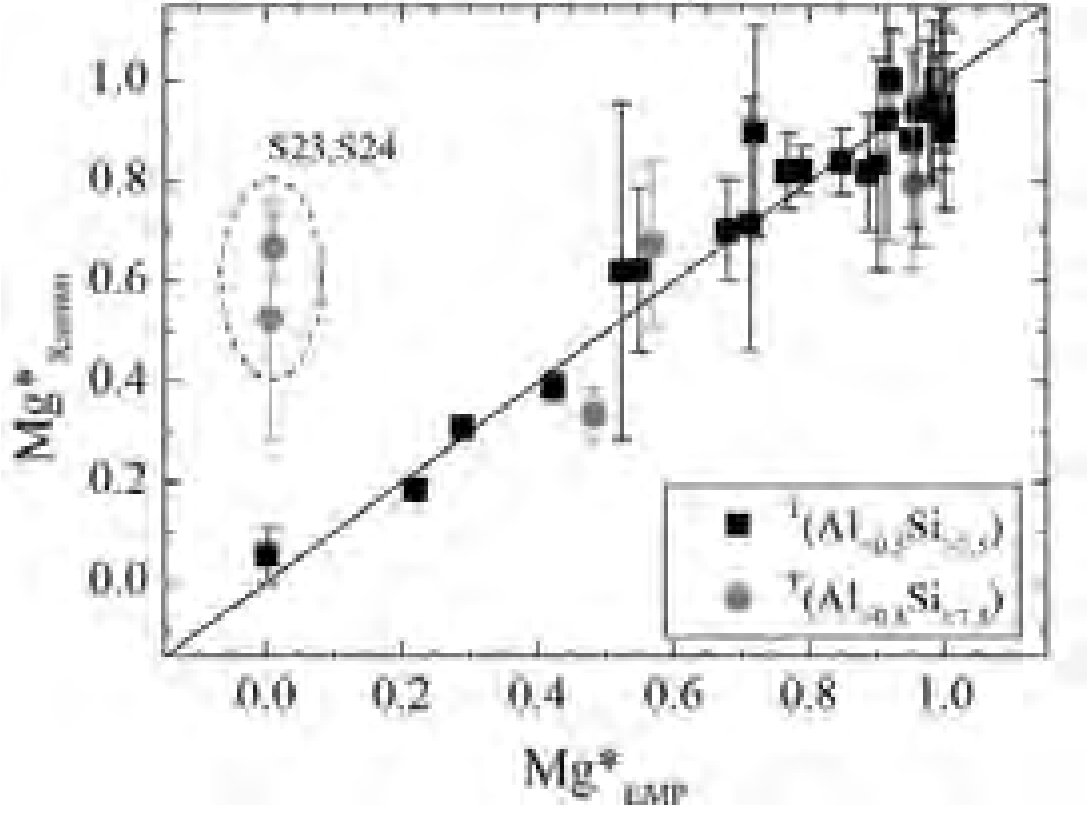
S23,S24
1.0
0.8
0.6
0.4
0.2
0.0
0.0
0.2
0.4
0.6
0.8
1.0
Mg*Raman
Mg*EMP
T1(Al0-0.4Si2.6-3)
T2(Al0-0.4Si3.6-4)

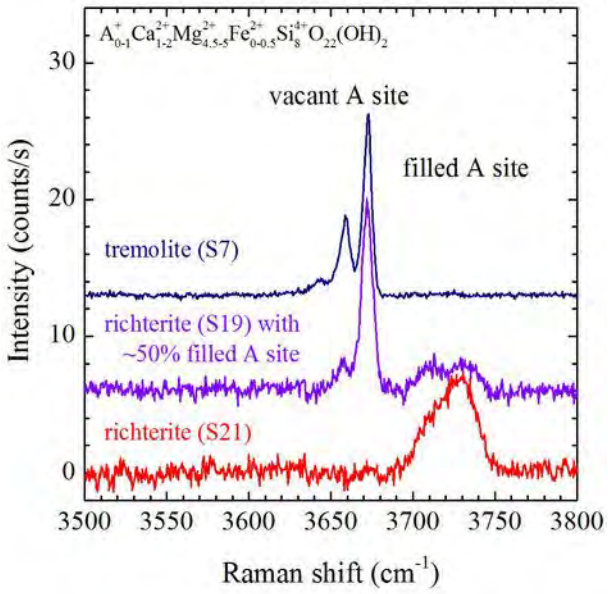
$A^{+}_{0-1}Ca^{2+}_{1-2}Mg^{2+}_{4.5-5}Fe^{2+}_{0-0.5}Si^{4+}_{8}O_{22}(OH)_2$
vacant A site
filled A site
tremolite (S7)
richterite (S19) with
~50% filled A site
richterite (S21)
Intensity (counts/s)
Raman shift (cm^{-1})
0
10
20
30
3500
3550
3600
3650
3700
3750
3800

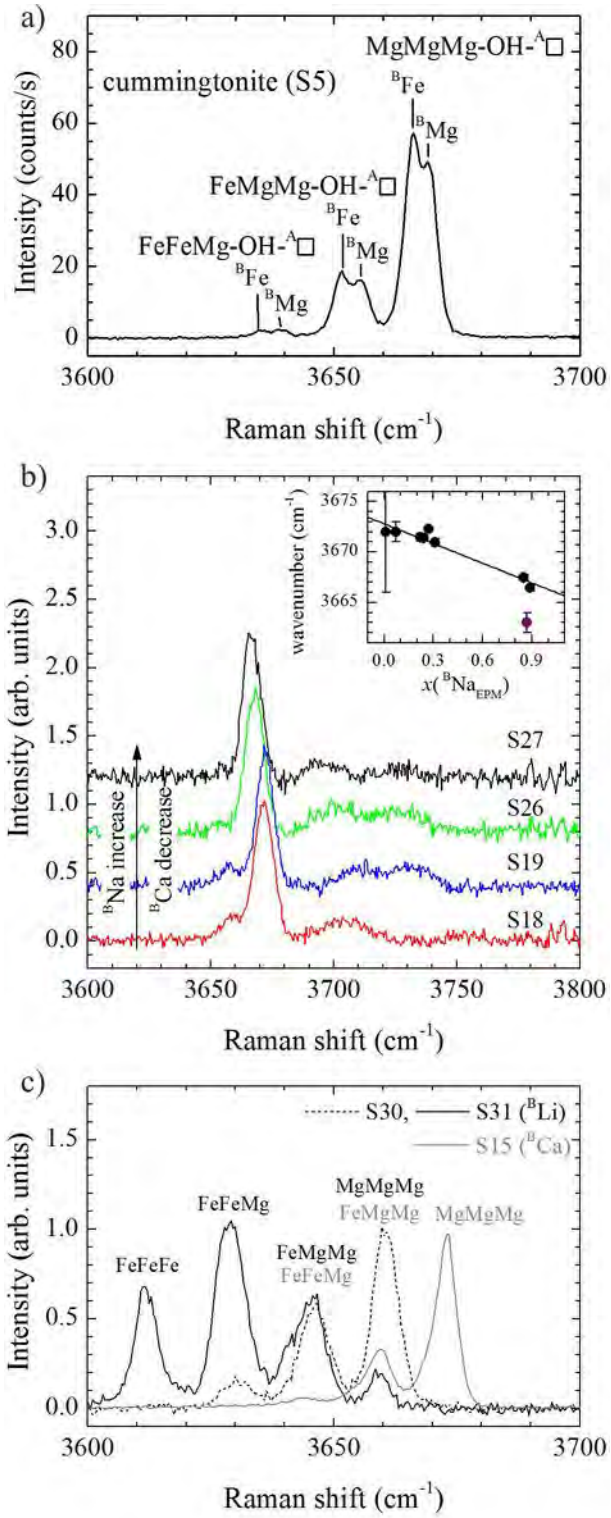
a)
cummingtonite (S5)
MgMgMg-OH-^{A}□
^{B}Fe
^{B}Mg
FeMgMg-OH-^{A}□
^{B}Fe
^{B}Mg
FeFeMg-OH-^{A}□
^{B}Fe
^{B}Mg
Intensity (counts/s)
Raman shift (cm^{-1})
b)
wavenumber (cm^{-1})
x(^{B}Na$_{EPM}$)
S27
S26
S19
S18
^{B}Na increase
^{B}Ca decrease
Intensity (arb. units)
Raman shift (cm^{-1})
c)
S30, S31 (^{B}Li)
S15 (^{B}Ca)
FeFeFe
FeFeMg
FeMgMg
FeFeMg
MgMgMg
FeMgMg
MgMgMg
Intensity (arb. units)
Raman shift (cm^{-1})

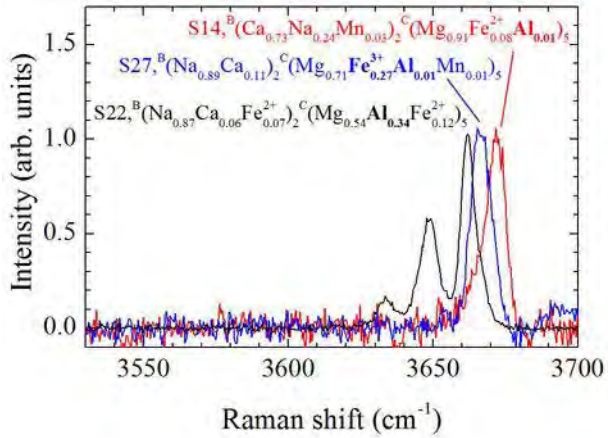
S14,B(Ca0.73Na0.24Mn0.03)2C(Mg0.91Fe2+0.08Al0.01)5
S27,B(Na0.89Ca0.11)2C(Mg0.71Fe3+0.27Al0.01Mn0.01)5
S22,B(Na0.87Ca0.06Fe2+0.07)2C(Mg0.54Al0.34Fe2+0.12)5
Intensity (arb. units)
1.5
1.0
0.5
0.0
3550
3600
3650
3700
Raman shift (cm-1)

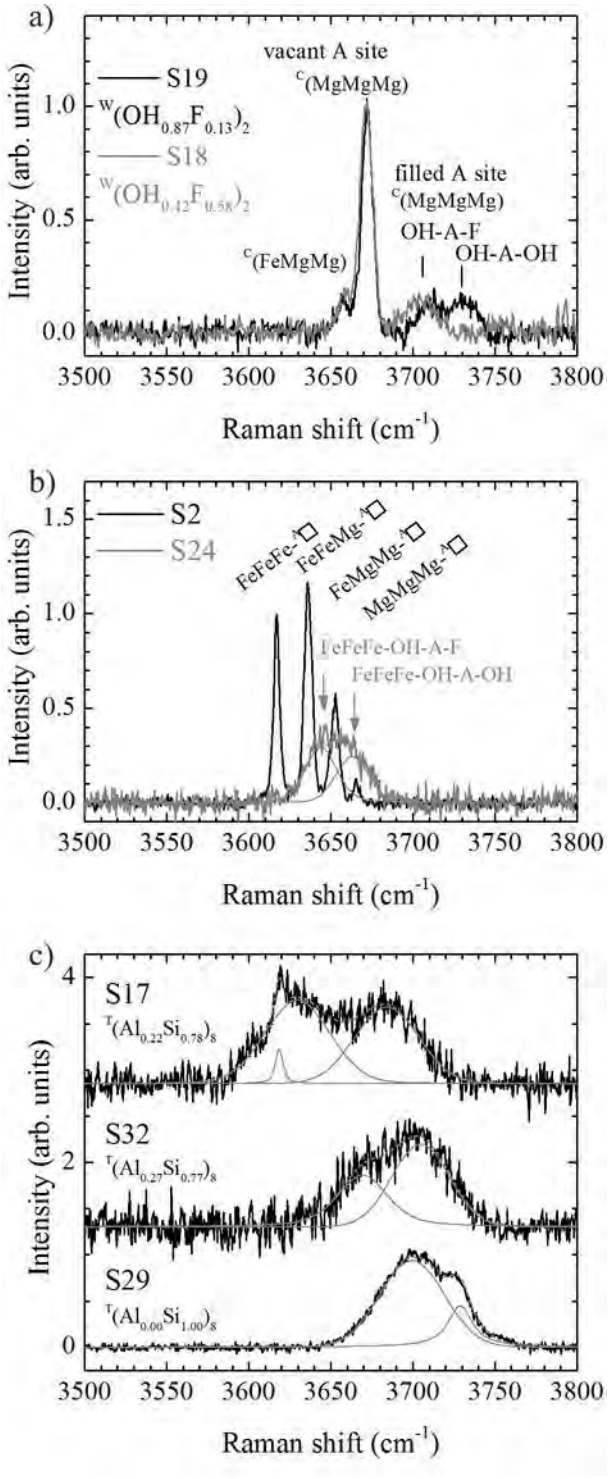
a)
S19
W(OH0.87F0.13)2
S18
W(OH0.42F0.58)2
vacant A site
C(MgMgMg)
filled A site
C(MgMgMg)
C(FeMgMg)
OH-A-F
OH-A-OH
Intensity (arb. units)
Raman shift (cm-1)
b)
S2
S24
FeFeFe-A□
FeFeMg-A□
FeMgMg-A□
MgMgMg-A□
FeFeFe-OH-A-F
FeFeFe-OH-A-OH
Intensity (arb. units)
Raman shift (cm-1)
c)
S17
T(Al0.22Si0.78)8
S32
T(Al0.27Si0.77)8
S29
T(Al0.00Si1.00)8
Intensity (arb. units)
Raman shift (cm-1)

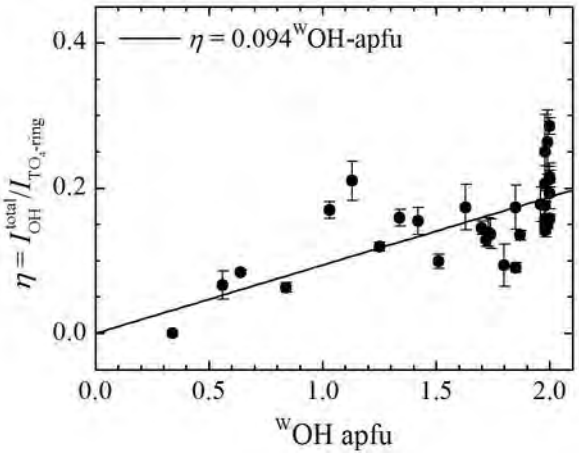
$\eta = 0.094^{W}$OH-apfu
$\eta = I_{OH}^{total}/I_{TO_4\text{-ring}}$
0.0
0.2
0.4
0.0
0.5
1.0
1.5
2.0
^{W}OH apfu

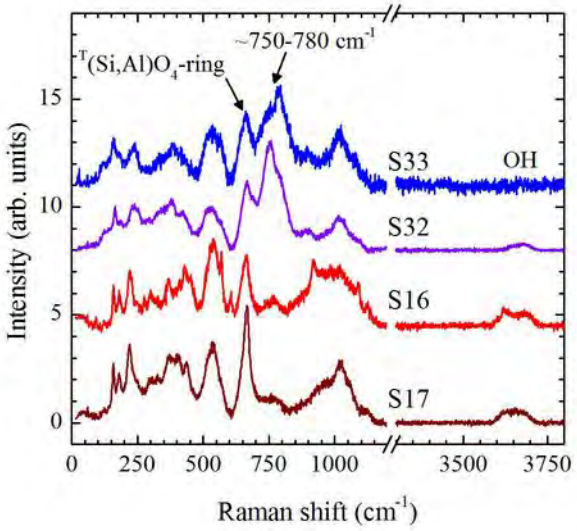
~750-780 cm-1
T(Si,Al)O4-ring
S33
OH
S32
S16
S17
Intensity (arb. units)
Raman shift (cm-1)
0
5
10
15
0
250
500
750
1000
3500
3750